

Raja Ramanna
Centre for Advanced Technology Indore



Annual Progress Report :2016-17

Raja Ramanna Centre for Advanced Technology, Indore
Annual Progress Report : 2016-17

Sr. No.	Contents	Page No.
I.	Indus Synchrotrons	2
II.	Accelerator Technology	12
III.	Laser Technology	20
IV.	Laser Applications	26
V.	Materials Science	34
VI.	International Collaboration	42
VII.	Infrastructure	43
VIII.	Human Resource Development	44
IX.	Outreach Activities	45
X.	RTI Details	46

I. INDUS SYNCHROTRONS

I.A. Indus accelerators: operation

The synchrotron radiation sources, Indus-1 and Indus-2 are being operated round the clock as a national facility for the synchrotron radiation (SR) user community. Indus-1 was operated at 450 MeV energy, 100 mA current, and Indus-2 was operated at stored current up to 200 mA at 2.5 GeV energy. The undulators U1 and U2 installed in 2015 in Indus-2 were successfully operated at enhanced beam currents in excess of 150 mA. The third insertion device, namely, the APPLE-2 undulator was commissioned this year with demonstration of enhancement in brilliance. It was also operated at a beam current in excess of 100 mA. A number of optimization steps were employed to re-establish operation of Indus-2 at 200 mA with reduced vertical aperture of vacuum chamber at the APPLE-2 undulator location. The machine was run at 2.5 GeV, 200 mA in user mode. Figures 1 and 2 depict the typical user mode operation of Indus-2 at 2.5 GeV energy.

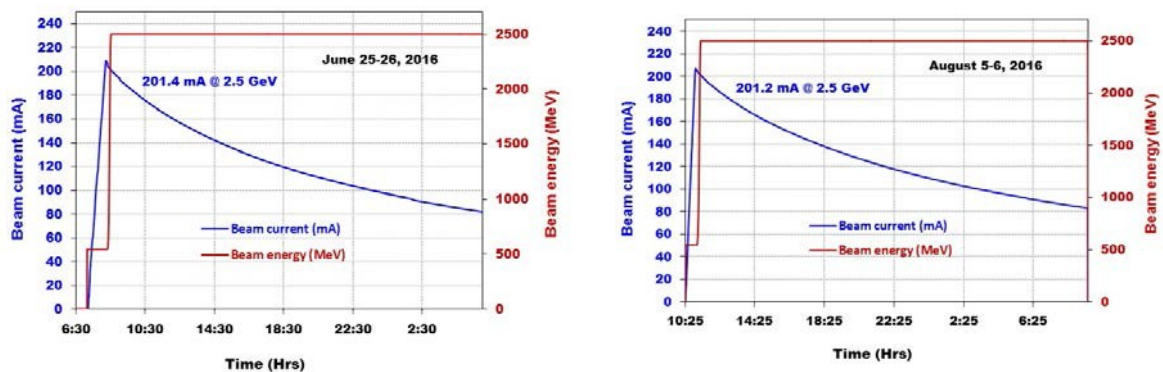


Fig. 1 and 2 : Indus-2 operation with ~ 200 mA stored beam current at 2.5 GeV energy.

Improvement in Beam Life Time

In Indus-2 the ceramic chambers of four injection kicker magnets were replaced with new upgraded chambers which has improved the vacuum in the injection segment from 3×10^{-9} mbar to 5×10^{-10} mbar. This has resulted in improvement in beam life time from ~ 20 hrs to more than 40 hrs at 100 mA beam current at 2.5 GeV beam energy. Figure 3 shows the graph of beam life time in Indus-2 during 2016. The lifetime has progressively improved after replacement of injection kicker chambers in April, 2016.

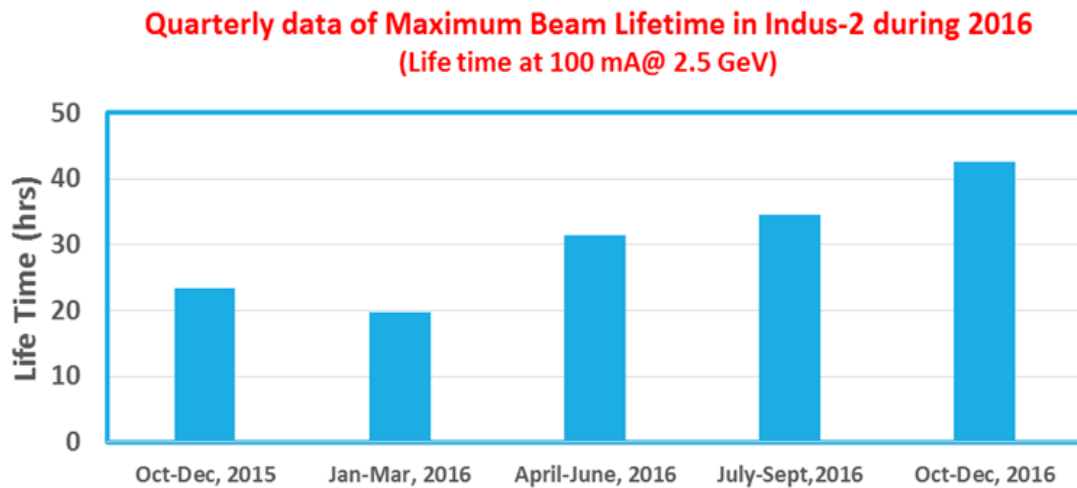


Fig. 3: Indus-2 beam lifetime.

The beam lifetime in Indus-1 also improved after the maintenance of UHV system carried out in April, 2016 which involved replacement of gate valve at Indus-1 and a number of titanium sublimation pump filaments in Indus-1 ring. During 2016, Indus-1 and Indus-2 were operated round-the-clock for 340 days. The beam availability to the users was more than 7200 hrs for Indus-1 and more than 5200 hrs for Indus-2.

I.B. Upgradation of Indus-2

I.B.1. Commissioning of advanced plane polarised light emitter (APPLE-2) undulator and Indus-2 operation at 100 mA with APPLE-2 vertical jaw movement

The Advanced Plane Polarised Light Emitter Undulator APPLE-2, was installed in Indus-2 last year. The effect of undulator action on the orbit stability with low beam current (~ 5 mA) at 2.5 GeV was studied. There was no significant distortion of the orbit during magnet pole gap and phase movement. The basic performance of the undulator was demonstrated using scanning wire monitor (SWM) and beam viewer mounted on the zero degree port of the downstream dipole magnet chamber.

The beam images of the SR coming from the undulator for 0 mm, $0.32\lambda_u$ and $0.5\lambda_u$ phase shifts corresponding to linear polarization in horizontal plane, circular polarization and linear polarization in vertical plane respectively are shown in figure 4. The observed beam profiles show a trend that matches well with the theoretical prediction.

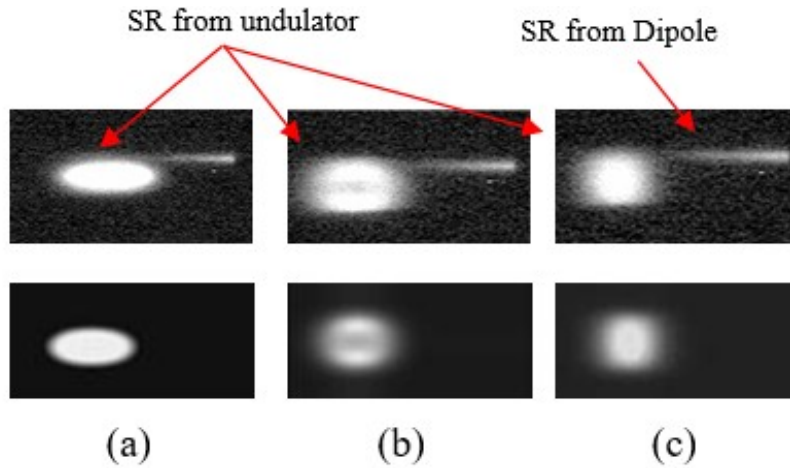


Fig.4: Beam profiles of the synchrotron radiation from APPLE-2 undulator for: (a) 0 mm phase shift (b) $0.32\lambda_u$ phase shift (c) $0.5\lambda_u$ phase shift. Top row: observed profiles. Bottom row: theoretical profiles. Both show a good match.

The circular polarized synchrotron radiation from this undulator will be used for the study of magnetic materials using by carrying out x-ray magnetic circular dichroism (XMCD) experiments in a dedicated beamline. The photon energy range of interest is 300 eV to 1500 eV including higher harmonics. After commissioning of the APPLE-2 undulator Indus-2 was operated at higher current (2.5 GeV, 100 mA) with vertical jaw movement of APPLE-2 up to minimum pole gap. There was no significant change in beam life time and temperature of vacuum chamber by changing the pole gap from maximum to minimum.

I.B.2. Operation of undulators U1 and U2 with 150 mA stored beam current at 2.5 GeV

The two planar undulators namely U1 and U2, installed last year in the Indus-2 storage ring were successfully operated at 150 mA, 2.5 GeV. In order to handle the high heat load of synchrotron radiation emitted from these undulators, the cooling water flow rate in the beam dumps was increased from 1.5 lpm to 3.5 lpm. All the components of the front end were re-aligned to ensure proper passage of beam without any obstruction. The safe limit of electron beam position were determined at low current and fed to the insertion device beam position indicator (IDBPI) interlock controls. Undulator operation was performed with beam current increase in steps. Tune variations during U1 and U2 undulator gap variation were measured, and it was observed that there was no significant change in betatron tune values during the undulator operation. It was also observed that there was no significant change in the temperature of vacuum chamber, and beam lifetime during the undulator pole gap variation. This demonstrated satisfactory functioning of sub-systems, interlocks and orbit correction schemes. During this experiment the jaws of APPLE-2 were wide open at maximum pole gap.

I.B.3. Upgradation of the power supplies of Indus-2

Four units of 60 A, 25 V power supplies for the quadrupole magnets of transport line (TL-2) have been installed. Four such supplies were installed last year. All the 8 power supplies have been successfully integrated with the new control racks. This complete the upgradation of the TL-2 quadrupole magnet power supplies. Three power supplies have been developed, installed and commissioned in Indus-2 magnet power supply hall. Eight fast orbit feedback (FOFB) corrector power supplies (third phase) for fast correction of electron beam orbit, and four active shunt power supplies for independent adjustment of Indus-2 quadrupole currents have been installed. The FOFB were recently used in the successful commissioning of Apple-2 undulator.

I.B.4. Upgradation of beam diagnostic system of Indus-2

An upgraded fluorescent type beam profile monitor (BPM) has been developed and three numbers of such BPM have been installed in the Indus-2 for the observation and measurement of electron beam profile. The design of BPM includes synthesis of newly designed linear actuation mechanism and ceramic support system, ultra-high vacuum compatibility, thermal and structural analysis of ceramic screen and structural analysis of it's housing and support. In order to keep the compatibility with the existing system of operation and control, the upgraded BPM uses the pneumatic system. However to make it fail safe (to avoid fluorescent screen coming in to the beam path in the event of pneumatic system failure), double acting pneumatic cylinders are used.



Fig. 5: Photographs of BPM and bellow assembly during lab test.

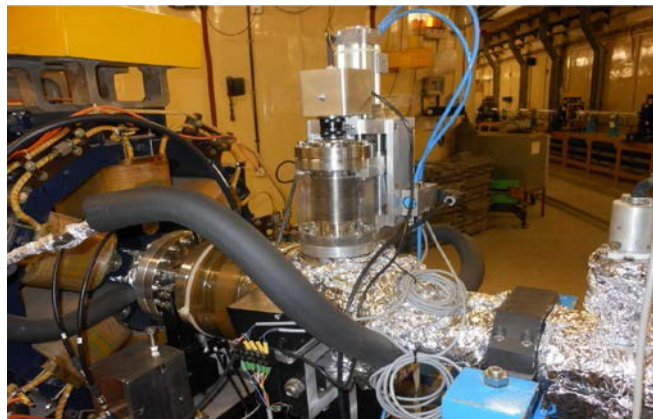


Fig. 6: Beam Profile Monitor installed in Indus-2 ring.

Upgraded beam position indicators (BPIs) have developed and six units were installed in Indus-2. The upgraded BPIs have improved features like transfer impedance $\sim 0.56 \Omega$ @ 505.8 MHz (targeted value $> 0.5 \Omega$), sensitivity ~ 0.06 per mm (targeted value > 0.05 per mm) in both the transverse planes and dedicated vibration isolation support structure. Software

development for bunch-by-bunch betatron tune measurement has been carried out to obtain the information about betatron tune of individual electron bunches in Indus-2.

I.B.5. Improvement in the performance of coolant system of Indus accelerator complex in low conductivity water (LCW) plant

In an accelerator like Indus-2, low conductivity water (LCW) is used for the cooling of accelerator components, power devices in magnets and RF power supplies etc. Heat dissipation depends on the performance of secondary loop containing soft water circulation through plate heat exchanger and cooling tower in the circuit. Cooling is accomplished by water evaporation because of which concentration of dissolved solids takes place. A weak acid cation bed has been developed and installed for online polishing of cooling tower water. This has brought down the water hardness from 20 ppm to 2 ppm. Further dosing of 98% sulfuric acid at the rate of 120 ml per hour has been started. As a result, scale formation is found to have been controlled.



Fig. 7: Weak acid cation bed.



Fig. 8: Acid dosing system.

I.B.6. Gas bremsstrahlung studies in Indus-2

Usually, gas bremsstrahlung dose for electron storage ring is simulated for air at atmospheric pressure and is scaled to the actual pressure (\sim nTorr) to estimate the radiation source term. For the simulation, composition of air is used in which percentage of N_2 is highest (78%) followed by O_2 (21%) and remaining, other gases. In the actual case, the residual gas in a storage ring is different than the air composition. Residual gas data obtained from residual gas analyser (RGA) from undulator section (U2) of Indus-2 storage ring was analyzed and gas bremsstrahlung simulation study was performed for both air composition and the measured composition of residual gas molecules from Indus-2 ring. The gas bremsstrahlung spectrum and dose rate (arising from interaction of 2.5 GeV electrons with gas molecules from the straight vacuum section of 1 m length of the storage ring) in a tissue

phantom were studied and composition of the residual gas from the storage ring using FLUKA code.

The absorbed dose rate normalized to pressure in the ring was found to be 1.249 Sv/h-nTorr in case of air composition and 0.392 Sv/h-nTorr in the case of residual gas composition for 2.5 GeV and 200 mA circulating current.

Effect of gas molecules like hydrogen, nitrogen, oxygen, CO₂, CO, air, residual gas from Indus-2 on gas bremsstrahlung spectrum and corresponding doses were also studied. The absorbed dose rate obtained is found to increase with the product of effective atomic number and molecular mass of gases.

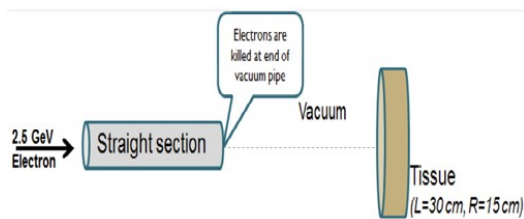


Fig.9: Geometry used for gas bremsstrahlung dose simulation.

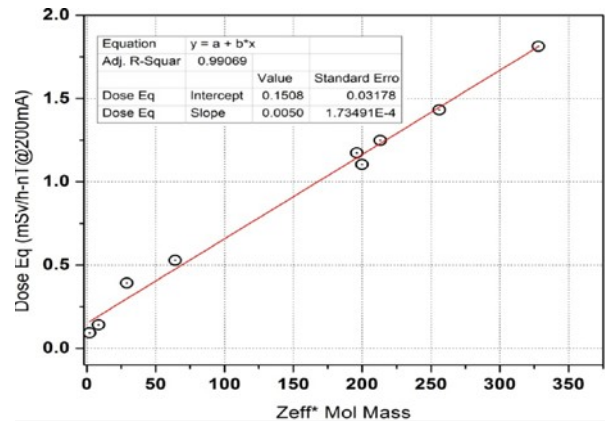


Fig. 10: Dependency of Dose Equivalent with residual gas composition.

I.B.7. Radiation shielding evaluation for insertion device beamline

Indus-2 has been upgraded with the addition of three undulators (insertion devices). Source term evaluation studies for undulator beam line in Indus-2 were performed using FLUKA Monte Carlo code. The simulation for shield assessment for the beam line was carried out by incorporating relevant beamline components like mirror, mirror chamber and complete optics hutch layout. The necessary front and lateral wall thickness for the hutch was found to be 5 mm and 2 mm thick (lead) respectively to contain the scattered bremsstrahlung photons. Additional 15 cm polyethylene is also suggested behind the bremsstrahlung stop to provide shielding for neutrons generated from the bremsstrahlung stop. The dose rate in the detectors are found to be within acceptable level.

I.B.8. Indigenous development of broadband kicker RF cavity for longitudinal multi-bunch feedback system (LMBFS) for Indus-2:

In storage ring Indus-2, at high beam currents longitudinal instability of the beam adversely affects the machine performance like saturation in beam accumulation, partial or

complete beam loss during the beam energy ramping and increase in the beam size. These instabilities can be controlled by implementing longitudinal multi-bunch feedback system (LMBFS). A broadband (1264.5 MHz -1517.5 MHz) kicker RF cavity will be used in LMBFS for Indus-2 to provide longitudinal kick to tackle instabilities. An aluminum wide band (1264.5 MHz -1517.5 MHz) ridged waveguide loaded re-entrant type prototype kicker cavity has been designed, fabricated and tested. A complex geometry of waveguide loaded structure has been realized to get the low quality factor of 5.5 required for wideband application. RF characterization was carried out using a VNA, broadband two four-way splitters, eight cables of identical length and 50 Ω matched loads. Optimized cavity diameter and length are ϕ 162 mm and 230 mm respectively for a central frequency of 1391 MHz and the loaded quality factor 5.5. Tuning was performed by taking machine cuts cavity lip, thereby adjusting the cavity length iteratively along with measurements to arrive at the desired frequency. To take care of harmful higher order modes (HOM), three HOM damping loop type couplers are also designed and mounted. The resonant frequency, bandwidth and R/Q of all modes including fundamental are measured and found satisfactory for the purpose of curing longitudinal multi bunch instabilities of Indus-2.

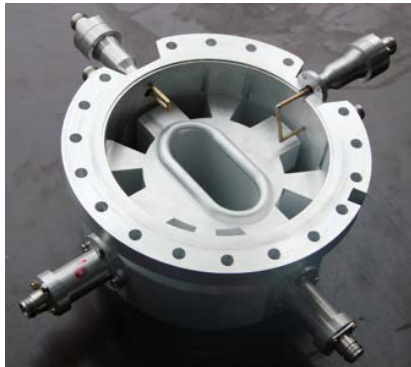


Fig.11: Half cell of kicker RF cavity.

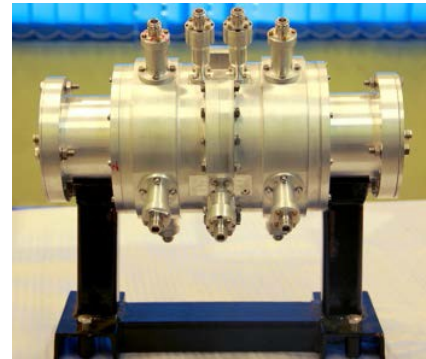


Fig.12: Assemble kicker cavity with couplers.

I.B.9. Upgradation of vacuum system of Indus-2

Modified four numbers of upgraded ceramic vacuum chambers for kickers in Indus-2 have been installed in Indus-2. This has improved the average vacuum of the Indus-2 storage ring and increase in beam life time to more than 30 hrs at 100 mA and 2.5 GeV. The average vacuum in the ring now is 3×10^{-10} mbar as compared to 9×10^{-10} mbar with the old ceramic chambers.

I.B.10. Development of upgraded Indus-2 injection thin septum magnet

A new injection thin septum magnet with a aperture (10 mm x 28.5 mm) has been developed. The thickness of septum with mu metal shield and 0.25 mm alumina coating has been optimized for radial field homogeneity ($\sim 10^{-3}$) near the thin conductor and low leakage

fields outside the septum towards circulating orbit. The magnet was fabricated from 0.1 mm NiFe C-shape laminations with assembly tolerances of better than $50\ \mu$ along the 250 mm length. The NiFe cores were annealed at $1100\ ^\circ\text{C}$ in the hydrogen atmosphere and oxidized on both surfaces so as to get $10\ \mu\text{m}$ electrical insulation to reduce eddy currents during pulse operation. On excitation with a $50\ \mu\text{s}$ pulse integral field homogeneity ($\Delta B/B$) was found to $\sim 3 \times 10^{-4}$ and the effective magnetic length was $\sim 250\ \text{mm}$. The maximum of the stray field is reduced down to 0.05% of the peak main field. The measured waveforms of stray field are in good agreement with the simulation results.

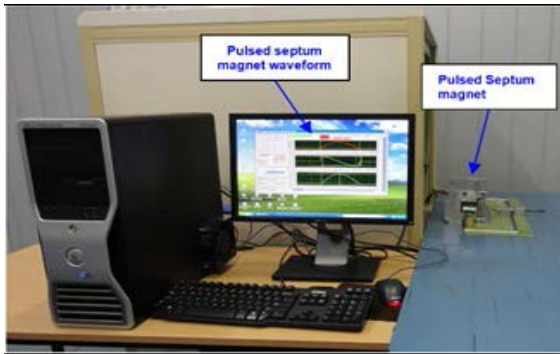


Fig.13: Thin septum magnet in the measurement bench.

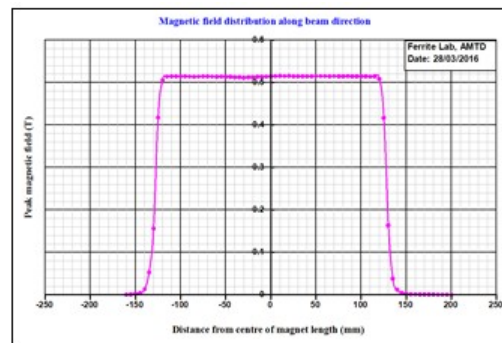


Fig. 14: Magnetic field distribution along septum length.

I.C. Indus beamlines utilization and up-gradation

I.C.1. 1. Indus beamline utilization

The 6 beamlines on Indus-1 and 13 (10 open to users) on Indus-2 are national facilities. More than 600 user experiments were carried out at the Indus-1 and Indus-2 beamlines in the calendar year 2016, leading to about 100 publications in peer reviewed international journals.

Some of the work carried out at the Indus-1 and Indus-2 beamlines is described briefly.

Studies on optical properties of low-Z/low-Z C/B₄C multilayers have been carried out using synchrotron based soft x-ray reflectivity beamline (BL-3) in Indus-1. These low electron density contrast (EDC) structures have potential to be used as mirrors, monochromators, beam splitters etc. for high intensity radiation. Resonant photoelectron spectroscopy experiments have been carried out using the angle resolved photoelectron spectroscopy beamline on Indus-2 in several systems including an intermetallic alloy FeAl.

The angle dispersive x-ray diffraction beamline (BL-12) was used to study various technologically important materials. Interface properties of NiO epitaxial thin films were studied. Nucleation and growth of the product phase was studied in the Fe_xRh_{1-x} alloy system and a phase co-existence was shown to occur in the temperature range of 300 K to 320 K.

Temperature dependent crystal structure was determined for multi-function materials Co_3TeO_6 and $\text{Co}_{2.5}\text{Mn}_{0.5}\text{TeO}_6$. A strong coupling between the spin and lattice degrees of freedom has been demonstrated in the materials.

Extended x-ray absorption and fine structure (EXAFS) measurements have been carried out on technologically important materials. In a study on CeO_2 , it was shown that Sm and Sr doping strongly favors local structural changes favorable for reducing the operating temperature of electrolytes for intermediate temperature (300 °C to 450 °C) operation, which is reported for the first time. EXAFS and XANES measurements were performed on Mn-Li co-doped ZnO nanoparticles. Their implications on the photocatalytic properties.

Soft x-ray absorption beamline BL-1 has been used for the study of oxygen absorption in niobium doped TiO_2 which is important for applications such as gas sensors, photocatalysis, electron injection in solar cells and alternative conductive electrode. The role of Nb doping in changing the Ti-O bond and Ti oxidation state was analyzed and correlated with the observed physical and optical properties. The protein crystallography beamline BL-21 has been used to solve several protein structures. Among them, the structure of Acylpeptide hydrolase enzyme from an extremely radiation resistant bacteria *Deinococcus radiodurans* has been solved and analyzed. The results may be relevant in the radiation resistant mechanism observed in the bacteria.

Total reflection x-ray fluorescence (TXRF) based x-ray absorption near-edge spectroscopy has been carried out at x-ray fluorescence beamline BL-16 to determine the oxidation state of uranium in mixed-valent U_3O_8 and U_3O_7 uranium oxides. The analysis revealed that U present in U_3O_8 is a mixture of U(V) and U(VI), whereas U in U_3O_7 is mixture of U(IV) and U(VI). The present study has demonstrated the possibility of application of TXRF for the oxidation state determination and elemental speciation of radioactive substances in a nondestructive manner with very small amount of sample requirement.

Monochromatic x-rays at an energy of 20 keV at the imaging beamline (BL-4) has been used for the formation of Ag nano-particles by the process of radiation induced hydrolysis. This is a novel technique used for the first time to produce bulk amount of nanoparticles. X-ray lithography beamline (BL-7) has been used for the development of several high aspect ratio structures for focusing x-rays and correcting the x-ray wave-fronts to get better focusing properties of mirrors. A large aperture lens, required for the x-ray diffraction beamline (BL-11) of Indus -2 was fabricated.

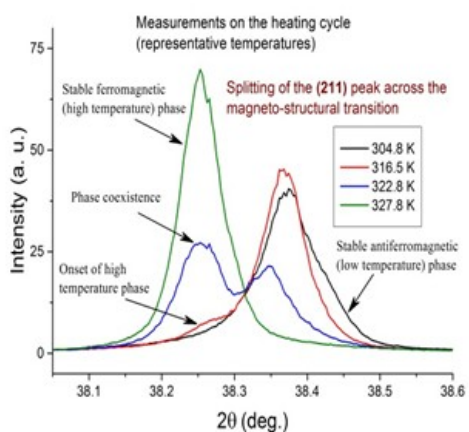


Fig.15: Diffraction patterns of Fe_xRh_{1-x} alloy showing phase coexistence.

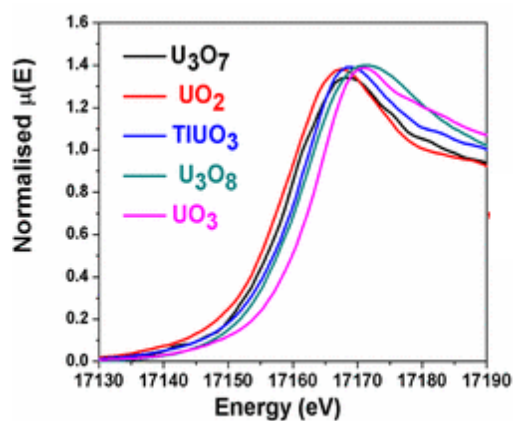


Fig. 16: The x-ray absorption data recorded in the TXRF geometry for different uranium samples.

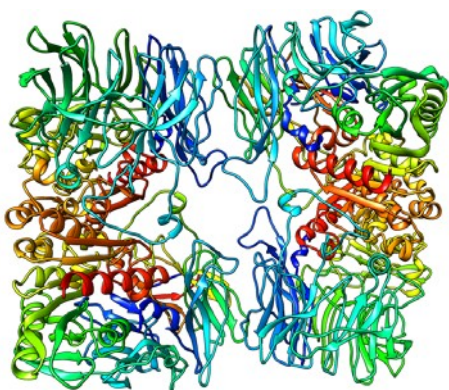


Fig.17 : Crystal structure of Acylpeptide hydrolase (close form) from *Deinococcus radiodurans* at 2.15 Å resolution.

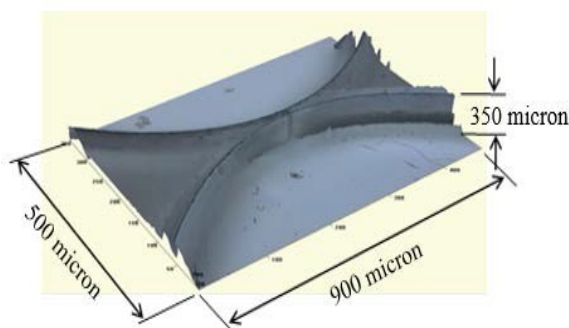


Fig.18: The optical image of the lens fabricated at the lithography beamline.

I.C.2. Development of beamline front ends

Significant efforts have been put in towards the development of new beamlines and their related facilities. These include the installation of the radiation shielding hutch of the Engineering applications beamline, installation of the monochromator of the ARPES beamline, procurement of the gratings and the other optical components for the ARPES beamline etc. The front end (FE) for Indus-2 soft x-ray beamline (BL-26) has been installed and tested. The major components like water-cooled shutter, safety shutter, collimator, vacuum chambers and support/alignment systems are designed, fabricated, tested and installed in Indus-2 ring. A vacuum of the order of 1.0×10^{-9} mbar has been achieved in the front end. Some of the components like pre-mask, water cooled beam viewer, scanning wire monitor etc. of undulator U-3 based x-ray magnetic circular dichroism beamline (BL-20) front end have been designed, indigenously fabricated and installed in Indus-2. The beam viewer and wire monitor are used to provide the shape, size, position and profile of the synchrotron

radiation from undulator U-3. A part of the front-ends for “Atomic, molecular and optical sciences beamline” (BL-5) on U-1 undulator and “Angle-resolved photo-electron spectroscopy beamline” (BL-10) on U-2 undulator have been installed as shown in figures 19 and 20. The remaining components of these front-ends like water-cooled shutters, safety shutters, water-cooled masks, beam viewer and vacuum chambers are designed, fabricated and tested for 1.0×10^{-9} mbar vacuum.

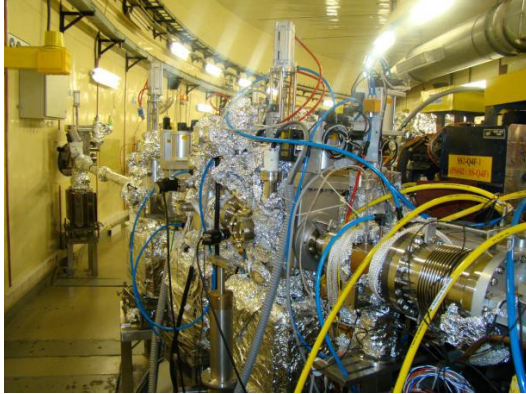


Fig.19: Front end part installed in BL-5 (Atomic, molecular and optical sciences beamline)

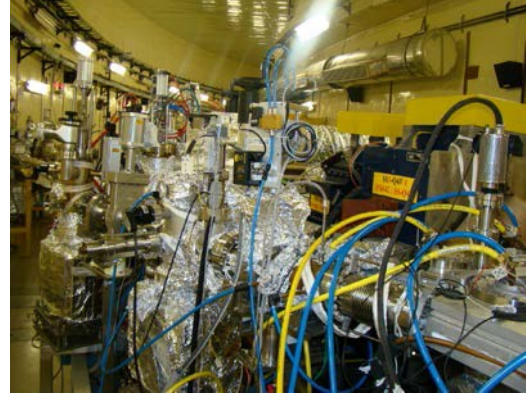


Fig.20: Front end part installed in BL-10 (Angle-resolved photoelectron spectroscopy beamline)

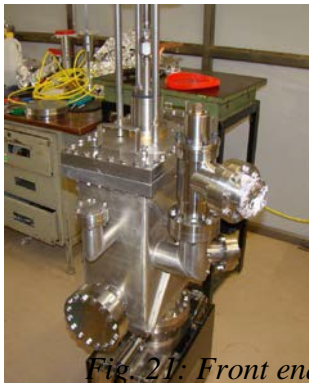


Fig. 21: Front end components of BL-5 and BL-10 beamlines for undulator U1 and U2.

II. ACCELERATOR TECHNOLOGY

II.1. Fabrication, processing and testing of 650 MHz beta=0.92 single-cell SCRF cavity

Facilities for fabrication, processing, and low temperature RF testing of superconducting radio frequency (SCRF) cavities have been set up at RRCAT including a large size centrifugal barrel polishing machine. A single-cell 650 MHz (Beta=0.92) superconducting cavity, TB9-RRCAT-304, was fabricated using the in-house electron beam welding facility. It was leak tested and barrel polished. Around 200 micron material was removed from the equator using ceramic, plastic and colloidal silica solution to remove surface defects and polish the internal surface of the cavity. The barrel polished cavity was

thermally processed at 600 °C for 10 hours in high vacuum using high temperature annealing furnace facility, specifically setup for niobium material. The last step of polishing was light electro-polishing to remove ~ 20 micron material using electro-polishing facility. After electro-polishing the cavity was ultrasonically cleaned. The cavity was rinsed with ultra-pure water at ~ 100 bar pressure and dried and prepared for 2 K testing in a class 100 clean room. Finally, the cavity was at 120 °C in oven in high vacuum. The cavity was tested using in the VTS facility at RRCAT. An excellent quality factor of 3×10^{10} was achieved with an accelerating gradient of $E_{acc} \sim 12.8$ MV/m.

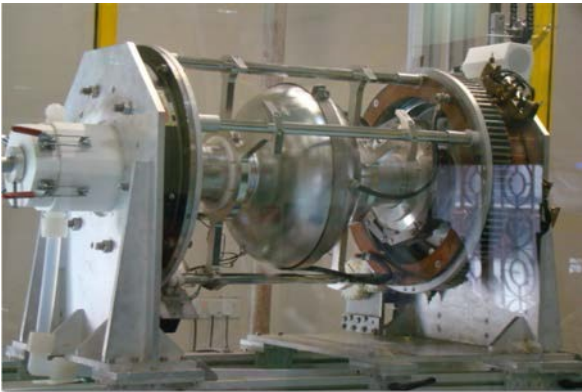


Fig.22: Electro-polishing of single-cell 650 MHz SCRF cavity.

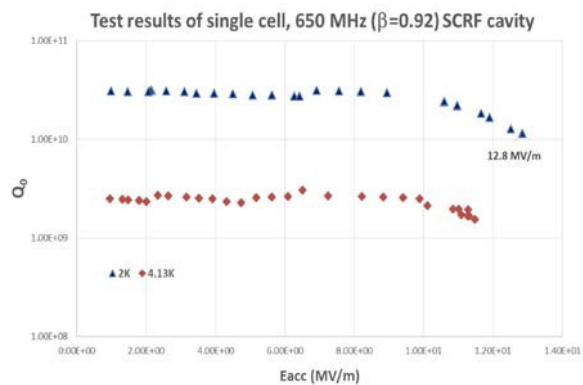


Fig.23 : Vertical Test Results for single-cell 650 MHz ($\beta=0.92$) SCRF cavity.

II.2. High beta 650 MHz five-cell SCRF cavity

RRCAT has initiated fabrication of HB 650 MHz ($\beta=0.92$) five-cell bare cavity. Design and fabrication of various cavity fabrication tooling and fixture like forming tooling, welding and machining fixtures have been completed. Component fabrication for first prototype five-cell SCRF cavity including half cells, beam tubes, flanges etc. have been completed. It is planned that the first prototype HB 650 MHz five-cell cavity fabrication shall be completed by March 2017. It will be subsequently taken up for its further processing and testing at 2 K for qualification. Such elliptical 650 MHz cavity with two different beta ($\beta= 0.61$ and $\beta= 0.92$) would be required for the superconducting proton linac for the DAE's two future major accelerator projects namely, ISNS and ADS.

II.3. World's first multi-cell laser welded SCRF cavity

SCRF cavities are highly expensive but essential components of high intensity particle accelerators. At RRCAT a 5-cell laser welded superconducting radio frequency (SCRF) cavity has been fabricated. This technology for fabrication of SCRF cavities, with laser welding

technique, has been developed for the first time in world. This replaces expensive electron beam welding technology, being currently used internationally for this application. This technology is a breakthrough in the fabrication technology of SCRF cavities as it will bring down the cost of fabrication of SCRF cavities very significantly. The feasibility of this technology was proved when the first single cell cavity fabricated by this technique at RRCAT was tested at Fermi lab and it gave a gradient of 31.6 MV/m at quality factor Q_0 of 1×10^{10} at 2 K. This is similar to the performance of a conventionally fabricated SCRF cavity. The technology has been granted patent in USA (US 9352416 B2) and Japan (Patent No. JP5632924).

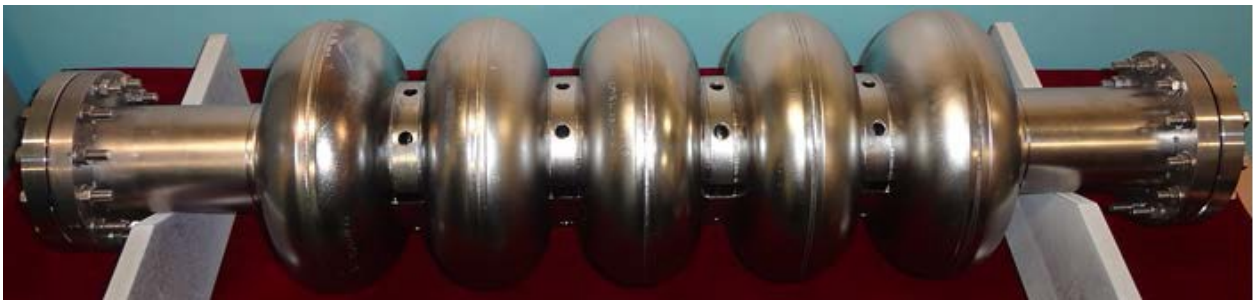


Fig : 24-cell laser welded superconducting radio frequency cavity.

II.4. Development of high voltage DC and pulse power supplies for IMS based explosive detection system being developed at ECIL

Explosive detection facility is an important requirement for the security of our nation. Presently India does not have any indigenously developed explosive detection system. ECIL Hyderabad and IGCAR, Kalpakkam took up the development of an Ion Mobility Spectrometry (IMS) based indigenous explosive detection system in the year 2012 under *Technology Development for India* for detection of explosives like TNT, RDX, PETN etc. High voltage pulsed and DC supplies required for the drift tube of the IMS detector were developed at RRCAT, Indore. The biggest challenge was to develop these supplies in small size which fits into the detector system. Various possible designs and topologies were studied and simulations were carried out. Prototypes based on various possible designs were developed, tested and studied. After several visits and interactions with ECIL, both, pulsed and dc supplies which met the electrical, electronic, thermal and mechanical specifications were developed. These supplies were integrated with the detection system replacing the imported supplies. The oxygen and TNT detection was then successfully carried out. The proposal from technology transfer for these power supplies in progress.



Fig. 25: Oxygen detection on detector's screen with RRCAT HV pulse and HV DC supplies.

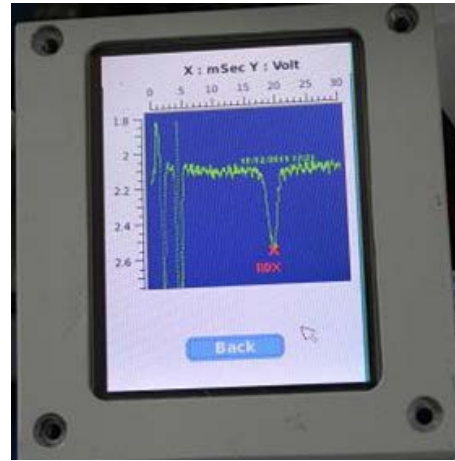


Fig. 26: TNT - RDX detection on detector screen with RRCAT HV pulse and HV DC supplies.

II.5. Development of high stability, high power capacitor charging power supply for future projects

This power supply will be used to charge pulse power circuit capacitors of septum / kicker pulsers at a repetition rate of 25 Hz. The capacitor charging power supply was designed and developed to charge 50 μF energy storage capacitor from 0 V to 2 kV within 35 ms, exhibiting a charging power of 2.8 kJ/s. The measured output voltage stability at 25 Hz was $\pm 0.01\%$.



Fig. 27: High voltage capacitor charging power supply during testing.

II.6. Development and testing of first 10 MeV, 5 kW electron linear accelerators (linac) at RRCAT

Raja Ramanna Centre for Advanced Technology, Indore has indigenously developed a 10 MeV, 5 kW electron linear accelerators (linac) for agricultural, medical, and industrial applications. The accelerating structure is traveling wave type and operates in S-band (2856MHz). The first linac has reached a power level of 5 kW in long duration operations. This linac is under beam characterization to be deployed at Agricultural Radiation Processing Facility being set-up at Indore.

The second linac of the series, with several refinements in engineering design, has been tested at a beam power of 1 kW following the stipulations of Atomic Energy Regulatory Board. It is now ready for long term endurance testing at a beam power of 5 kW.



Fig.28: First linac tested at beam power of 5 kW.



Fig. 29: Second linac tested at beam power of 1 kW.

II.7. Mutation-breeding of new crop varieties using electron beam irradiation performed at RRCAT

Ionizing radiation induced mutation breeding is an efficient tool for increasing the genetic variability for obtaining desired traits in crop like disease resistance, standing capacity in unseasonal rains, increase in productivity, drought resistance etc. Electron beam irradiation of rice and wheat seeds was done at RRCAT, using dual scattering system for obtaining the necessary low dose irradiation for Nuclear Agriculture and Bio Technology Division, BARC, Punjab Agricultural University, Ludhiana and Indira Gandhi Krishi Vishwavidyalaya, Raipur. Electron beam facility based on 10 MeV linac operating at RRCAT and delivering pulsed beam was used for the irradiation of these seeds.



Fig.30. Electron beam irradiation of rice and wheat seeds.

II.8. Infra-red free electron laser development

An indigenously developed infra-red free electron laser (IR-FEL) is being commissioned at RRCAT. It has a 2.5 m long pure permanent magnet undulator with 50 mm period, and an injector linac system capable of delivering a 15 MeV to 25 MeV electron beam. The accelerated electron beam from the injector system is transported to the undulator by an electron beam transport line that manipulates the round beam at linac exit to a flat beam with desired properties at the undulator entry. Electron beam diagnostics in the form of integrating current transformers (ICTs) and beam profile monitors (BPMs) are employed to monitor the electron beam properties at different locations of the IR-FEL setup. The high stability ($\pm 100 / \pm 400$ ppm) 13 A / 15 V power supplies required for the various magnets were designed at RRCAT. The production and testing was carried out by ECIL, Hyderabad. Installation, cabling and testing of 45 power supplies in local made was completed last year. This year the power supplies were interfaced with the central control room for remote operation. They have been in regular use for the past one year. The IR radiation generated in the IR-FEL setup is out-coupled through a 2.5 mm hole in the downstream mirror, and the out-coupled IR power is measured using a liquid helium cooled bolometer. The laser also requires RF signals of 29.75 MHz for electron gun, 476 MHz for sub harmonic pre-buncher (SHPB) and 2856 MHz for linac. For proper bunching and acceleration of the electron beam all RF signals need to be synchronized and phase locked. This indispensable phase locking between all three RF signal has been achieved in synchronized

signal generation unit, by deriving 476 MHz and 29.75 MHz RF signals from a 2856 MHz RF signal of RF synthesizer. RF power level of 29.75 MHz, 476 MHz, and 2856 MHz is adjusted to meet the requirement of electron gun pulsar, SHPB RF system and linac RF system respectively. These signals are successfully interfaced to the respective systems with satisfactory performance. The first signature of lasing at $\sim 34 \mu\text{m}$ wavelength has been successfully observed recently in the setup, with an estimated gain of $\sim 10^4$ over enhanced spontaneous emission during experiments with an 18.3 MeV electron beam with approximately 26 A peak micro-pulse current over a 5 μs electron beam macro-pulse. Further experiments are presently underway to achieve saturation of the FEL gain.

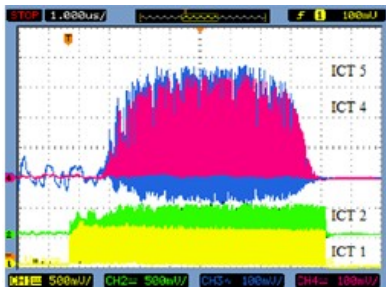


Fig. 31: ICT traces at different locations in the IR-FEL setup

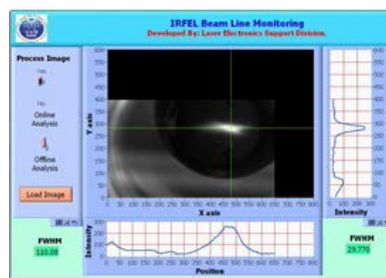


Fig. 32: Typical beam spot at undulator entry.



Fig. 33: Typical saturated bolometer trace during lasing.

II.9. End to end beam dynamics simulation studies for the 1 GeV H^- injector linac for Indian spallation neutron source (ISNS)

One of the very crucial aspects in the design of an injector linac for a spallation neutron source is to find out an optimum arrangement of different kinds of accelerating cavities and focusing magnets. This optimum arrangement should ensure that the beam is kept focused in the transverse as well as longitudinal direction over the full length of the linac. Since the beam power is very high (1 MW), there is a very stringent criterion on the fractional beam loss that can be tolerated to keep the induced radioactivity below the acceptable level such that the hands-on maintenance of the accelerator is possible. This puts several stringent beam dynamics criteria that need to be satisfied by the lattice of the linac.

An optimum lattice for the linac has been designed for the expected beam parameters at the exit of the ion source. The current design includes a 1.9 m long low energy beam transport (LEBT) section, 3.49 m long radio frequency quadrupole (RFQ) section, 3.68 m long mid energy beam transport (MEBT) section and 252 m long linac section comprising 20 nos. of single spoke resonator (SSR0) cavities, 28 nos. of SSR1 cavities, 48 nos. of SSR2 cavities, 54 nos. of mid beta cavities and 48 nos. of high beta cavities, along with solenoids and quadrupole doublets. Beam dynamics simulations have been done with this configuration and

it has been checked that all the stringent beam dynamics criteria are met.

II.10. Studies of power threshold of ferrite and garnets for high power circulators

The power threshold of ferrites is an important issue in design and development of high power CW circulators. At high powers, spin waves are excited in non-uniform mode. Power from RF field is then coupled into spin wave system leading to energy dissipation. The critical Power P_{crit} , at which spin wave resonance sets in line width is an important measurement required to determine the power handling of ferrite materials. A parallel pumping test bench has been developed to measure the non-linearity in microwave ferrite and garnets. It consists of pulsed power magnetron, TE_{104} cavity with ferrite spherical sample and a tunable electromagnet. RF power is applied parallel to the static magnetic field; at low power negligible microwave power is absorbed by the ferrite samples. Beyond a certain critical or threshold value there is an abrupt increase in the absorbed power level. This marks the onset of nonlinearity. 1 mm to 2 mm diameter spheres of yttrium garnets and I-CVG have been fabricated and tested in this system. No non linearity is observed in ferrite and garnets up to 100 kW in below resonance operation.

Based on above results, a ferrite disk resonator of 207 mm diameter and thickness of 5 mm at 505.8 MHz has been made using plural (triangle) ferrite pieces. The corner of each ferrite piece is ground in order to avoid discharge and gap of 1 mm is provided between two pieces. Tests of circulator performance at high power has been carried out by passing hot water surrounding disk resonator with stripline which resembles temperature rise of 80 °C on the ferrite surface. This is equivalent to 100 kW CW power operation.

The performance of the circulator is measured for three types of distribution of the applied field by varying the shape, size of the pole piece of an electromagnet. This experiment shows that the insertion loss and isolation are improved by applying the internal dc magnetic field. Garnet disk resonator have been tested in a coaxial geometry using VNA. Insertion loss of 0.2 dB and isolation of 28 dB have been observed at 505.8 MHz & 650 MHz. These studies have been very useful for tailoring the correct molecular engineering compositional design of microwave ferrite and garnets for indigenous development of high power CW ferrite circulator (> 100 kW) for RF systems of Indus-2 ring and 650 MHz ferrite circulator for proton linac.

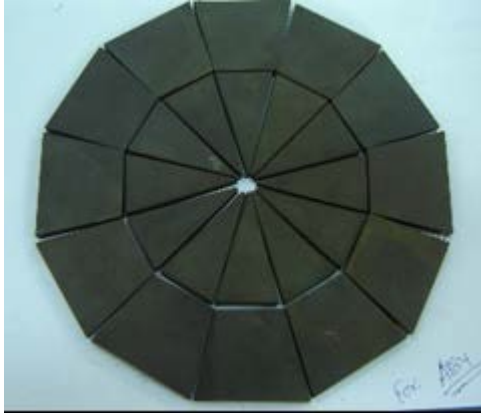


Fig. 34: I-CVG disk using plural pieces.

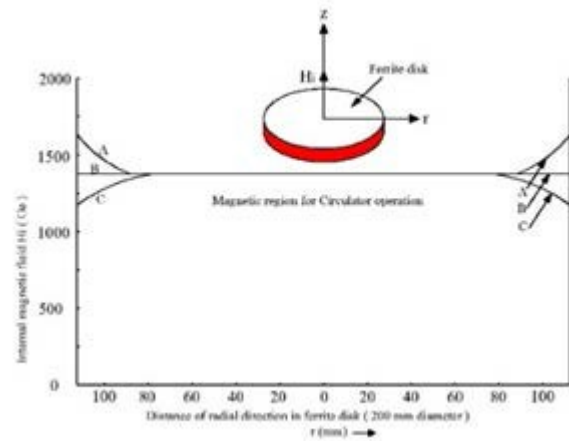


Fig. 35: Tuning of circulator with magnetic bias.

III. LASER TECHNOLOGY

III.1 Laser Development for Industrial Applications

The following lasers and laser based systems have been developed for industrial applications including nuclear reactor refurbishment and applied R&D:

III.1.1. Development of a compact Nd:YAG laser system for laser welding of brachytherapy assemblies

An Nd:YAG laser system based on compact ceramic reflector and single flash lamp pump chamber has been developed. The laser provides maximum pulse energy of 12 J in 10 ms pulse duration having laser beam diameter of 4 mm. Output pulse energy can be varied from 0.5 J to 12 J by variation in flash lamp current. Its pulse duration and repetition rate can be varied in the range of 2 ms to 10 ms and 1 Hz to 4 Hz, respectively. For this system, a compact 500 W average power pulsed power supply with controllers is developed. An electrical to laser conversion efficiency of 2.5% has been achieved with a pulse-to-pulse stability of better than 5%. The laser system is equipped with dual port fiber optic beam delivery through 200 μm core diameter optical fibers on time sharing basis. This laser system will be used for leak tight welding of high dose rate brachytherapy assemblies of miniature size (80 μm wall thickness, 1 mm diameter) at BRIT, Mumbai. One of the fiber ports will be used for welding in hot cell and second port for welding outside hot cell using a real time CCD camera based viewing system.

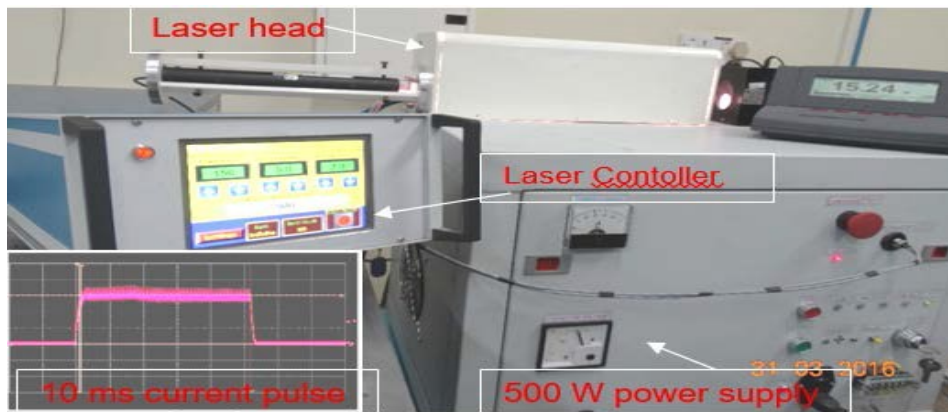


Fig. 36: In-house developed compact Nd:YAG laser system of 12 J pulse energy.

III.1.2 Development of a 630 W average power pulsed Nd:YAG laser with ceramic reflectors for use in hot cells of PIED, IGCAR

A double-lamp ceramic reflector based pump chamber and Nd:YAG laser system providing a maximum average output power of 630 W and 13 kW peak power in ms time duration has been developed for laser cutting of irradiated FBTR components in hot cell at IGCAR. Laser pulse duration can be varied in the range of 2 ms to 40 ms and pulse repetition rate from 1 Hz to 100 Hz. An electrical to laser conversion efficiency of 6.3% has been achieved, which is the highest reported worldwide for similar laser systems. Yellow glazed ceramic reflector based pump chamber is expected to enhance life of pump chamber to ~5 years as compared to 1 year for earlier used gold coated elliptical reflector based pump chambers. Resonator length is also reduced to 0.71 m as compared to earlier resonator length of 1.4 m for similar output power. Due to smaller resonator length, mechanical stability has been improved, which resulted in pulse-to-pulse stability of $\pm 3\%$ as compared to earlier value of $\pm 5\%$. Beam quality factor M^2 also improved to a value of ~ 83 as compared to earlier value of ~ 120 . A single unit power supply of 10 kW average power and a laser controller to drive two lamps synchronously with maximum 5 kW electrical input to each lamp has been developed. Laser output has been delivered through an optical fiber of 600 μm core diameter with 90% transmission efficiency. This high power laser has also been equipped with three energy/time shared ports for providing simultaneous three linear cuts to fuel tubes for dismantling of fuel assemblies. The laser system will be commissioned at IGCAR for laser cutting of FBTR components in hot cell in a radiation field of 10^6 Rad/hr.

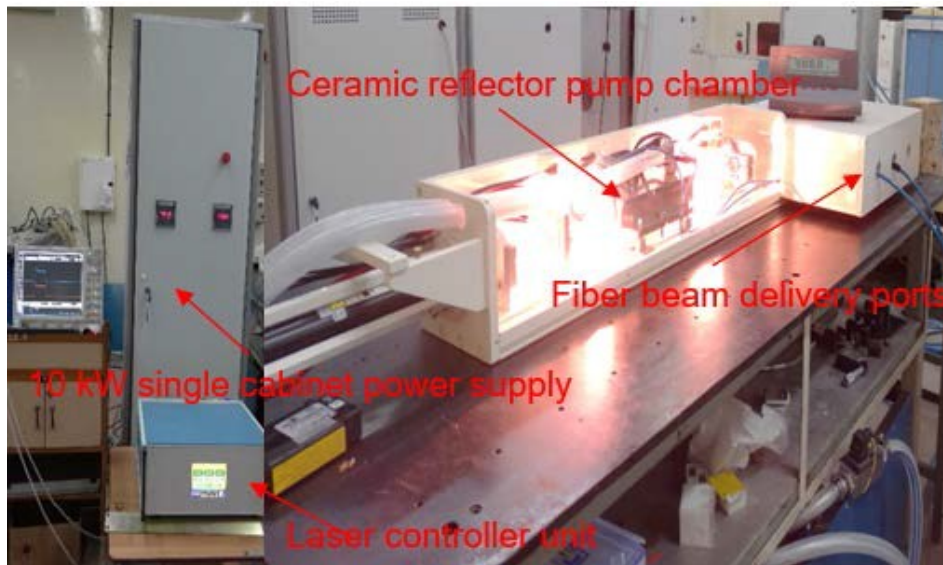


Fig. 37: A view of in-house developed 630 W average power pulsed Nd:YAG laser.

III.1.3. Development of laser radiator unit for defense applications

As a part of the indigenization effort to replace the imported technology, RRCAT has designed and developed a prototype laser radiator unit for defense applications, for laser guiding of a missile fired from a tank. The laser consists of an arc-lamp pumped continuous wave (CW) Nd:YAG laser emitting in the near infrared region of wavelength 1064 nm. The electrical and mechanical parameters of laser are matched to the imported laser. The required output power of laser is 13 W with pulse duration of up to 20 sec. The highly efficient prototype laser radiator unit developed at RRCAT delivered an output power of 25 W with water as coolant and 15.5 W with special coolant having low freezing point, for the same pulse duration which is more than 20% of the requirement.

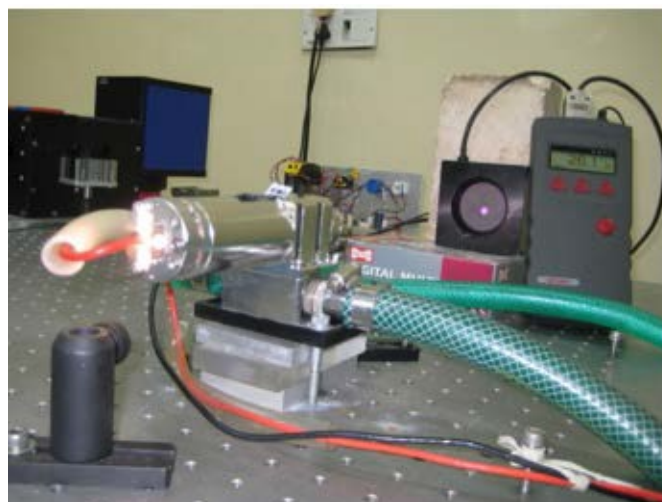


Fig. 38 The photograph of the laser radiator unit.

III.2. Development of various fiber lasers

An all-fiber thulium doped CW fiber laser (TDFL) has been developed with stable CW output power of 18 W using in-line fiber Bragg grating mirrors with a slope efficiency of 45% and centered at 1940 nm with sub-nanometer line width. These lasers have wide applications in material processing of metals and non-metals, surgery, defense and space applications. Laser output is emitted from 12 μm core diameter of thulium-doped fiber with half angle divergence of 140 mrad.

A mode-locked Ytterbium (Yb) doped fiber laser has been developed under stretched pulse configuration by implementing a grating pair inside the cavity for control of dispersion. The laser produces highly stable train of mode-locked pulses at 45 MHz repetition rate of duration 500 fs which were compressed to less than 50 fs duration with energy of 3 nJ in an external grating compressor. Two in-fiber polarization controllers (PC1 and PC2) were placed near collimators (COL1 and COL2) in combination with the polarization beam splitter. The mode locking in the oscillator is observed by biasing the polarization controllers.

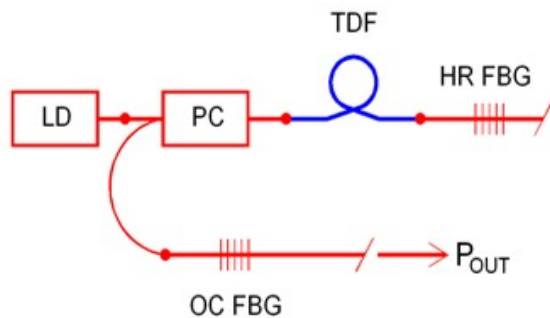


Fig. 39: A schematic view of 18 W Tm-doped all-fiber CW fiber laser.

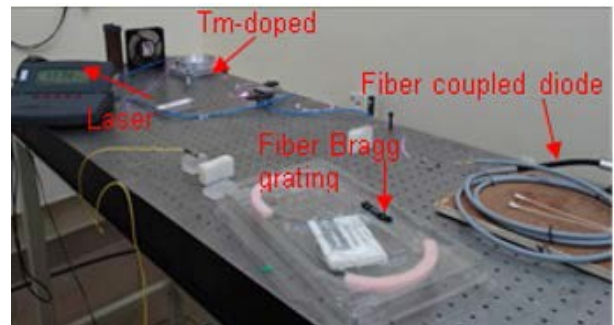


Fig. 40 : Table-top view of Tm-doped CW fiber laser.

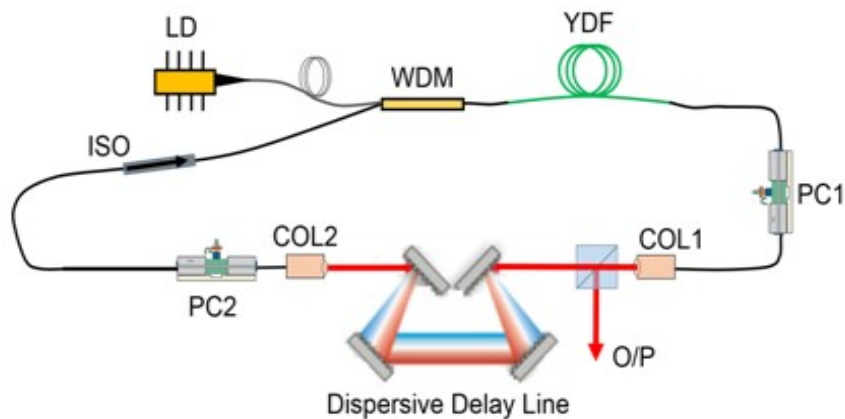


Fig.41: Schematic of stretched pulse Yb-oscillator.

III.3 Frequency doubled CW fibre laser with ~5W power at 515 nm

A lab model of frequency doubled narrow-line-width CW Ytterbium-doped fiber laser (YDFL) emitting ~5 W at 515 nm with narrow line width of ~0.07 nm has been developed for dye pumping applications. The laser is developed in two stages. The first stage of laser system is YDFL emitting 1030 nm radiation, which is based on all-fiber architecture for alignment free ruggedness. This stage provides linearly polarized CW output power of 20 W in narrow line width of 70 pm, which is within the spectral full-width at half maximum (FWHM) of non-linear crystal for efficient SHG. The slope efficiency in terms of absorbed pump power is more than 70%. About 5.5 W of output power at 515 nm has been generated with SHG conversion efficiency of ~25% using this set-up. This laser has a potential to replace Ar-ion lasers operating at this wavelength for pumping of Dye lasers.

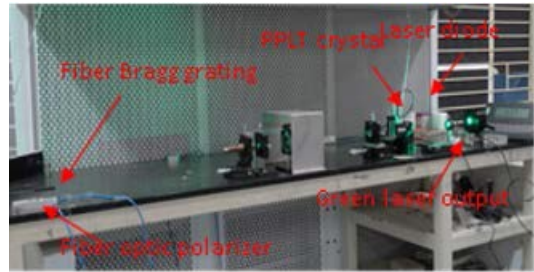
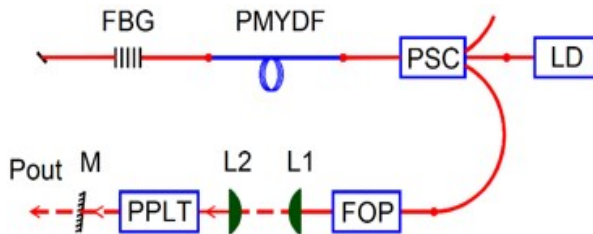


Fig. 42(a): A schematic view of 5 W green CW fiber laser at 515 nm.

Fig.42(b): Table-top view of green fiber laser.

III.4. Development of pulsed blue laser source at 456 nm

Pulsed blue lasers operating in spectral range of ~450 nm to 460nm have their great importance in special applications such as communication between aircraft and submarine and under water communication. A table-top model of high power pulsed blue laser source operating precisely at 456 nm wavelength has been developed. The laser provides average output power of ~ 1.2 W in pulses of duration 400 ns at 20 kHz repetition rate. Pulsed blue laser source precisely at 456 nm finds potential application for deep sea under water communication. Fiber coupled diode laser with 28W of maximum power and central wavelength of 808 nm at 25 °C was used as the pump source. The Z-shape laser resonator consists of a-cut Nd:GdVO₄ laser crystal along with an acousto-optic Q-switch modulator. For intra-cavity frequency doubling a LBO crystal was used for efficient frequency conversion. The output power was measured using a power meter after appropriate filters to block the residual pump and fundamental IR power.

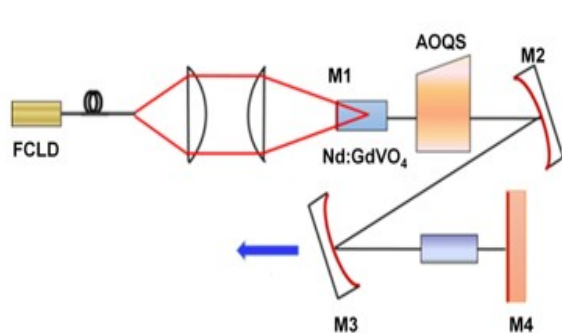


Fig. 43. (a) The schematic of the experimental setup.

Fig: 43 (b) shows a photograph of the blue laser under operation.

III.5. Development of all solid state RF powered 2 kW axial flow CO₂ laser system

A 2 kW RF-excited fast axial flow (FAF) CO₂ laser has been developed for material processing application. A noteworthy feature of the laser system is its excitation with an all solid state modular RF power (SS-RFPS) source. Modular RF power supplies can be pulsed from 100 Hz to 30 kHz giving pulse mode laser output at lower frequencies up to 1 kHz and quasi-continuous at higher frequencies of operation. Pulse mode operation provides dynamic power control option which is very important for laser material processing applications.

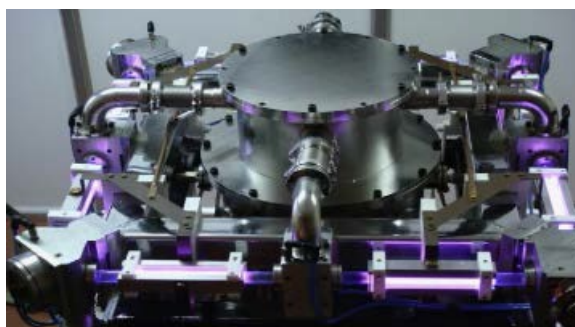


Fig. 44: 2 kW RF-FAF CO₂ laser (left) and RF discharge in four sections of the laser (right).

III.6. Development of Four Engineered Model of DPSS green lasers

Last year two numbers of engineered version of diode-pumped solid state (DPSS) green laser systems were developed and installed at Hall-6, BARC for pumping of dye laser amplifier chain. The DPSS lasers were successfully used for several long hour campaigns for resonance ionization experiments. This year four more such DPSS green lasers are to be delivered. The DPSS green laser system was a specially designed Q-switched intra-cavity frequency doubled Nd:YAG laser to obtain short pulse duration under high repetition rate. At a pump power of ~400 W, more than 40 W of average green power was obtained at 6.25 kHz repetition rate corresponding to pump to green conversion efficiency of ~10.5%. At the maximum output power the green pulse duration (FWHM) was measured to be ~40nsec. Four such engineered models of DPSS green lasers are ready to be delivered at BARC.

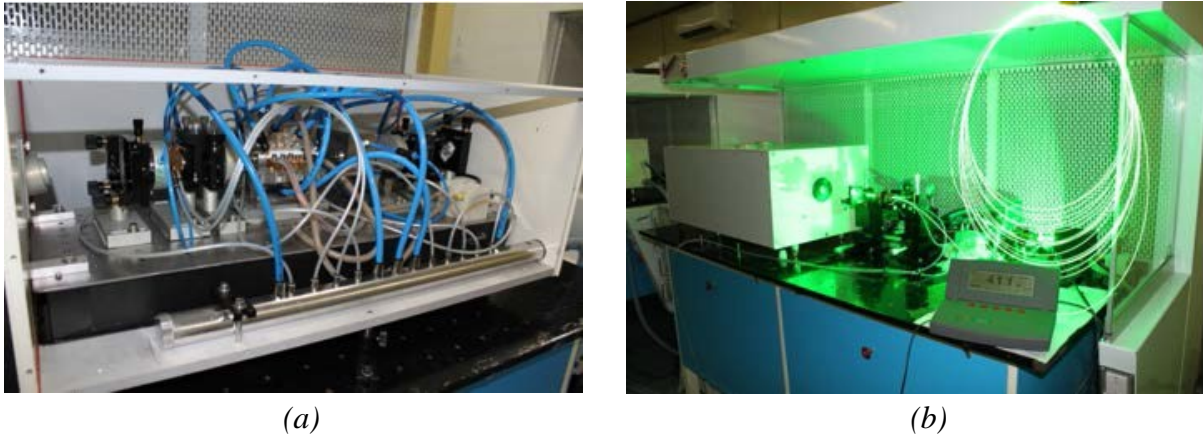


Fig: 45: Diode pump solid state green laser (a) Internal layout of DPSS green laser head and (b) DPSS green laser under operation with fiber coupling.

IV. LASER APPLICATIONS

IV.1. MoU for development of laser cutting and welding technology for nuclear reactors:

An MoU has been agreed between RRCAT and NPCIL for development and deployment of remotely operable laser systems and advanced laser cutting techniques for refurbishment of nuclear reactors. The MoU includes the development of 250 W Yb-doped CW fiber laser, four number of 5 kW average power Nd:YAG laser power supplies for high average power Nd:YAG laser systems. Different laser cutting tools and fixtures will be developed and deployed for in-situ refurbishing of Indian nuclear power plants in highly radioactive environment. As a part of MoU development of 250 W CW fiber laser are in progress.

IV.2. In-situ laser cutting of Q-15 and N-6 coolant channels from KAPS-2 reactor

Earlier, laser cutting technology was developed and deployed for removal of Q-16 coolant channel from KAPS-2 reactor in September-2015 due to leakage of heavy water near rolled joint portion of pressure tube after 20 years of commercial operation. From post-irradiation examination (PIE) of Q-16 coolant channel pressure tube and its stubs, it was found that along with cracks, corrosion is also present. Thus, Atomic Energy Regulatory Board (AERB) asked to examine nearby Q-15 pressure tube for any corrosion related issue. This pressure tube was also found to have corrosion and AERB asked to remove one more coolant channel N-6 for confirmation of presence of corrosion. Laser cutting technology was deployed again for removal of pressure tube and pressure tube stubs from rolled joint area. This coolant channel was obstructed by five feeder pipes and it was difficult to approach its bellow lip weld joint for laser cutting and its separation from calendria. Laser cutting tools for liner tube (4 mm SS410) and end fitting (11 mm thick SS410) from inside of the tube were

deployed and outboard end fitting was removed successfully. Another remotely operated miniature tool for laser cutting of bellow lip weld joint using laser cutting nozzle in two opposite orientations was deployed successfully and inboard end fitting was removed. After removal of inboard end fittings underwater gas-jet assisted laser cutting technique was deployed successfully to retrieve 5 pieces of PT stubs of 180 mm length from both sides of end fittings in a radiation field of ~ 700 Rad/hr for PIE analysis of pressure tube and its stubs from rolled joint area. Future operation of this reactor or en-masse coolant channel replacement (EMCCR) will be decided on the basis of PIE data of N-6 pressure tube and its stubs. For these laser cutting operations, in-house developed remotely operated fiber coupled Nd:YAG laser of 250 W average power was utilized.

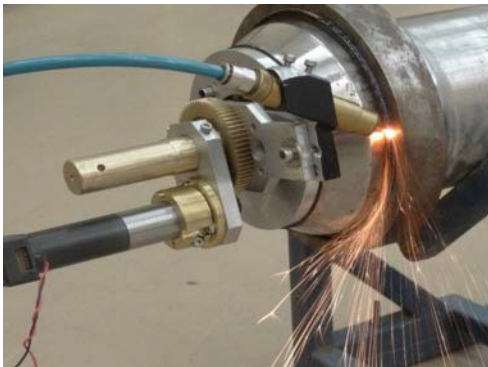


Fig. 46: Mock-trial for laser cutting of bellow lip after removal of outboard end-fitting.



Fig. 47: laser cutting tool for liner tube and end-fitting.

IV.3. Development of distributed temperature monitoring system using in-house fabricated fiber bragg grating (FBG) distributed sensors

Distributed fiber Bragg grating (FBG) sensors are developed for monitoring temperature at multiple locations with spatial resolution of 10 cm. The FBG sensors are inscribed on a photosensitive optical fiber, utilizing in-house developed FBG inscription facility. The FBG sensors have sensitivity of typically $10 \text{ pm}/^\circ\text{C}$ and temperature measurement accuracy of 1°C over a wide range upto 500°C . Online temperature measurement of ultrahigh vacuum chamber for Indus-2 synchrotron radiation source is a tough task because of presence of high electromagnetic interference (EMI). For this application a seven point FBG based distributed temperature monitoring system is developed using FBG interrogator to measure the temperature with resolution of 1°C . The FBG based temperature monitoring system is advantageous in term of reliable measurement in presence of high EMI, more accurate temperature measurement and faster response time as compared to conventional system.

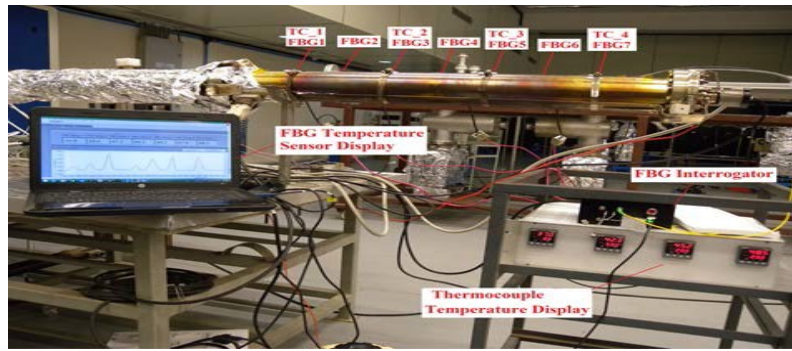


Fig. 48: Monitoring of temperature of Indus-2 UHV test set up using FBG based distributed temperature sensor.

IV.4. Design and development of a Raman probe for measurement of artifact-free Raman spectra from (*in-vivo*) tissues

A Raman probe is an important component of a Raman system intended for non-invasive tissue analysis. The presently available commercial Raman probes are not well suited for applications related to tissue analysis, because they introduce several artifacts which interfere with the Raman signatures appearing in the fingerprint region of the tissue Raman spectra thereby leading to confusion in its interpretation. A hand-held Raman probe capable of measuring artifact-free tissue Raman spectra was designed and developed. The design minimizes the fiber and optics generated Raman artifacts, optimizes collection efficiency, and has resulted in highly efficient Raman probe that is capable of collecting high-quality spectral data with a few seconds of acquisition time (Fig. 49). The performance of the probe was found to be better than the two commercially available Raman probes (one of Visionex make and the other of in photonics make) in measuring the artifact free Raman signal from biological samples. The capability of the probe for measuring artifact-free Raman spectra is evident from the quality of the measured Raman signal which is comparable to that measured open-air with a bench-top Raman system.

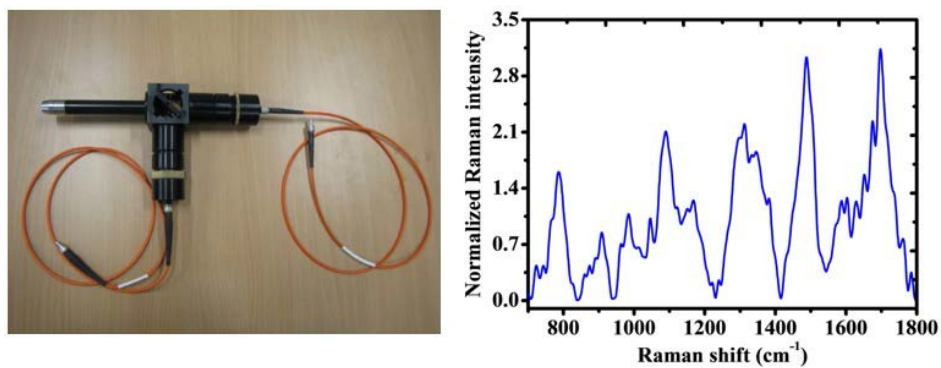


Fig. 49: The developed hand-held Raman probe and the *in-vivo* Raman spectrum measured from human palm using the probe.

IV.5. Raman spectroscopy and optical coherence tomography for investigating human oral mucosa

A clinical study was carried out at Tata Memorial Hospital (TMH), Mumbai on healthy volunteers and patients with oral cancer to evaluate the efficacy at Raman spectroscopy in oral cancer diagnosis. It was concluded that for accurate classification of oral lesions the reference normal database should exclude spectral data of tobacco using healthy subjects. An *ex vivo* imaging study of human oral tissue samples using the spectral domain polarization sensitive optical coherence tomography (PC-OCT) showed that the tissue birefringence derived from the OCT images provided more sensitive monitoring of the neoplastic transformation of oral mucosa.

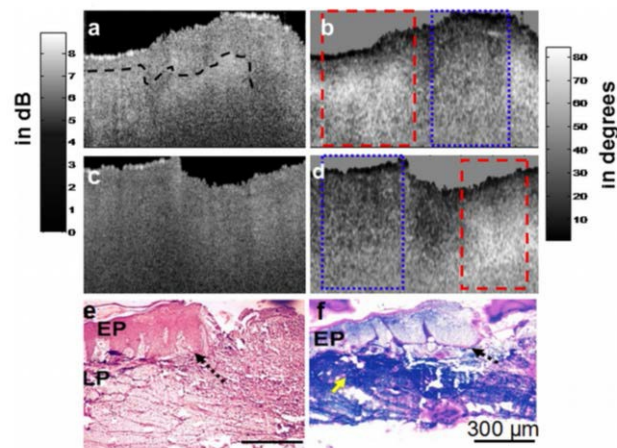


Fig. 50: OCT intensity (a, c) and retardation (b, d) images along the boundary of cancerous lesion. Normal and cancerous regions are marked by red dashed and blue dotted rectangles, respectively, in retardation image. Representative micrographs of HE-stained section (e) and trichrome stained section (f) for the boundary region. dashed arrows: region beyond which there is loss of basement membrane, Yellow arrow: Collagen fibers.

IV.6. Off-confocal Raman spectroscopy (OCRS) for depth-sensitive measurements of layered turbid samples

A novel technique of depth-sensitive Raman spectroscopy was developed for non-destructive sub-surface interrogation of layered turbid samples using the concept of varying Raman collection zones while keeping the point of illumination fixed on the surface of the target sample. The system adopts the experimental configuration of a confocal Raman, but employs off-confocal Raman detection for probing depths beyond the reach of the conventional confocal Raman. It allows subsurface interrogation by moving the tip of the Raman detection fiber (acting as the pinhole aperture) from the focus of the Raman collection objective either by taking the point of detection away from the objective (positive confocal offset) or bringing it closer to the objective (negative confocal offset). The ability of the system to recover Raman spectra of the subsurface layer was demonstrated using a layered non-biological phantom and a biological tissue sample.

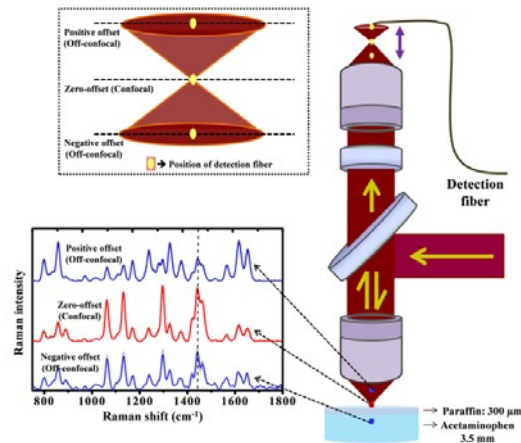


Fig. 51: Experimental setup for off-confocal Raman spectroscopy. Raman spectra measured from a non-biological phantom at confocal and off-confocal positions.

IV.7. Development of orthogonal polarization spectral imaging system

A setup based on orthogonal polarization spectral imaging was developed and its efficacy was demonstrated in measuring high contrast *in vivo* images of the vasculature network and blood flow through the micro capillaries in animal model. The system comprises a blue (450 nm) and green (530 nm) LED excitation source. The collimated excitation light is polarized horizontally using a linear polarizer before passing through a lens L which focuses it on to the sample. The light passing through the analyzer is then imaged on to a CMOS camera using the combination of lens L1 and L2. The analyzer placed in orthogonal polarization channel helps in eliminating the specular reflection and polarization maintaining components from superficial layers. The validation and optimization of the system on animal models is under progress.

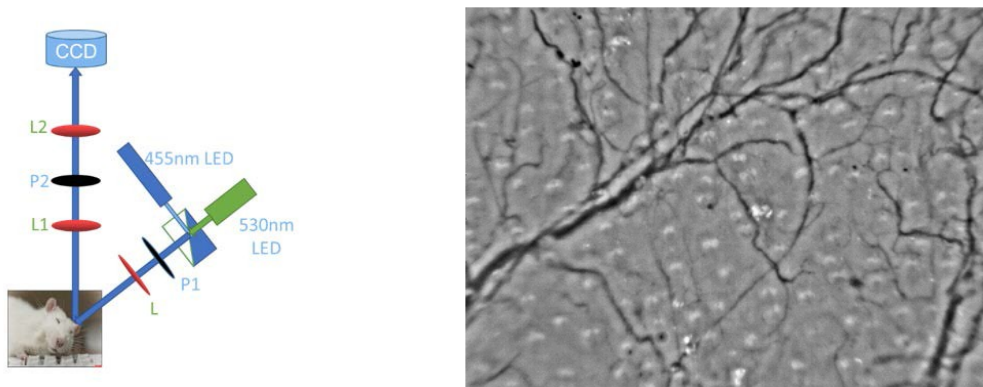


Fig. 52: A schematic of the orthogonal polarization spectral imaging setup for *in-vivo* imaging of micro-vasculature in animal model (left) and vasculature network in mouse ear (right). Image area 2mm x 2.5 mm.).

IV.8. Ultrafast shadowgraphy using high harmonic generation (HHG) Source:

The extreme ultraviolet (XUV) source based on high order harmonics of ultra-short Ti:sapphire laser pulses (pulse duration ~ 45 fs) possess unique characteristics viz. sub-fs time structure and simultaneously multiple discrete frequencies in XUV to soft x-ray regime, which can be used to estimate atomic/ionic density of the plasma plume at multiple wavelength resulting into more accurate estimation of the plasma density in single-shot. An experiment study on ultrafast shadowgraphy of carbon plasma plume using higher harmonic source (sub-fs) for mapping of atomic / ion density has been carried out. The high order harmonics were generated by focusing 45 fs laser pulse in plasma plume formed by focusing an uncompressed 200 ps laser pulse on the carbon target derived from the same laser pulse. The carbon plasma plume which is to be probed was also formed by focusing a part of the uncompressed 200ps laser beam, so that the harmonic beam generated from the first plume can directly pass through the second plume.

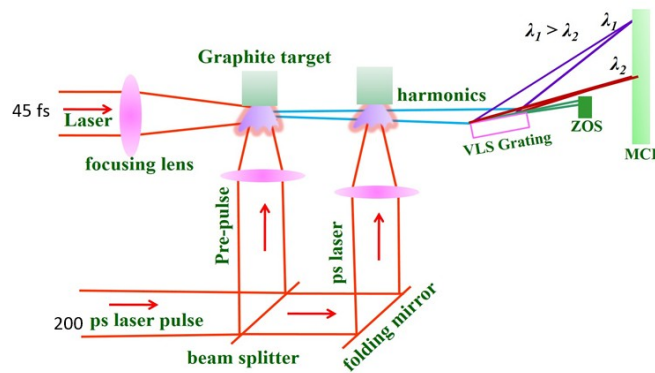


Fig. 53: The schematic of the experimental setup.

The plasma density mapping was carried out simultaneously using multiple wavelengths from 11th to 21st harmonic orders (wavelength range 72.7 nm to 38 nm). The probing of the plasma plume using multiple wavelengths provides an accurate density measurement in both high as well as low density regions simultaneously. The density was measured at different time delays from ~ 10 ns to ~ 80 ns of plasma evolution. The shadowgraphy of fast expanding plumes with ultrashort pulses results in low hydrodynamic blurring and provides sharp shadow grams. The transmission of the harmonics with and without formation of second plasma plume was. A significant intensity variation across spatial profile of the HHG spectra for the different harmonic order (11th to 21st harmonic order) is observed.

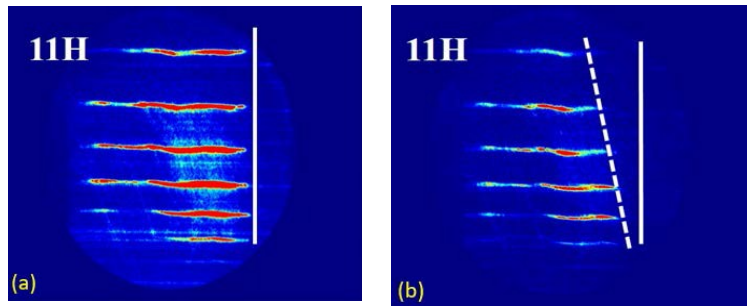


Fig. 54: Harmonic spectra transmitted through **a)** without plasma plume, **b)** with plasma plume.

From the penetration depth of different wavelengths of the harmonics and its transmission through the plasma, atomic density of the plasma plume is determined. This set of observations were also recorded for different delays between the HHG source and the plasma plume in order to observe the plasma density evolution with time as shown in figure 55.

The ion expansion speed in carbon plasma plume was measured to be $\sim 10^4$ m/s. The size of harmonic beam at the position of plasma plume was measured to be ~ 2 mm. It was observed that at smaller delay (~ 10 ns), the density gradient was observed to be very sharp. The carbon ion density varies from $\sim 6 \times 10^{19}$ cm^{-3} close to target surface to $\sim 3 \times 10^{17}$ cm^{-3} at a distance of ~ 300 μm away from the surface. As the delay increases the density gradient becomes shallow. At larger delay (~ 80 ns), the carbon ion density was measured to be $\sim 4 \times 10^{18}$ cm^{-3} at a distance of ~ 300 mm which was reduced to $\sim 2 \times 10^{17}$ cm^{-3} at ~ 2 mm away from the surface.

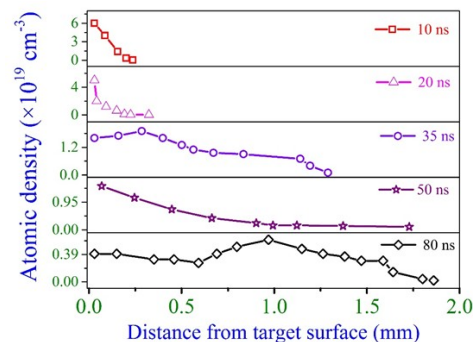


Fig. 55: Temporal and spatial variation of the plasma density derived from the transmitted HHG spectra through plasma plume.

IV.9. Development of a magneto-optical trap for Rb atoms on atom-chip

A magneto-optical trap (MOT) on the atom-chip for alkali ^{85}Rb atoms has been developed and made operational. An atom-chip is a plane reflecting surface of gold coated (thickness ~ 200 nm) Si-substrate (28 mm x 24 mm x 0.5mm) with a thin wire structure enscripted on it for magnetic trap formation after flowing current through wires. A photograph of in-house developed setup for atom chip-MOT is shown in figure 56(a). This atom-chip is

attached to a chip-mount assembly (length~ 472 mm) [figure 56(b)] and placed in an octagonal MOT-chamber at a pressure of $\sim 1 \times 10^{-8}$ torr with Rb-vapor in the background. The chip-mount assembly holds atom-chip and also provides electrical connections to copper strips to generate necessary magnetic field for MOT. Three laser beams in a reflection geometry on the atom-chip surface along with appropriate dc magnetic field make the MOT for cooling and trapping of atoms near the chip surface. In this MOT, cold cloud of ^{85}Rb atoms was observed at a distance of ~ 3 mm vertically below the surface of the atom-chip. The CCD camera image of the cold atom cloud trapped in the atom-chip MOT is shown in figure 56(c). The number of cold atoms in the MOT atom cloud was $\sim 2 \times 10^5$ at an estimated temperature of ~ 350 μK .

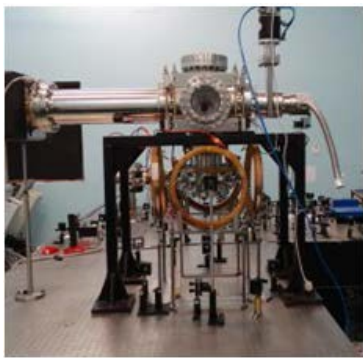


Fig.56(a): The experimental setup for Rb atom-chip MOT.



Fig 56(b): The chip-mount assembly.

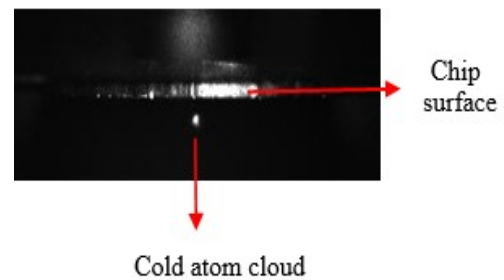


Fig 56(c): CCD camera image of the cold atom cloud near the chip surface.

IV.10. Development of high average power laser marker

A compact laser marker system with high average power of 18 W using diode-end-pumped Nd:YVO₄ gain medium has been designed and developed. The complete system was successfully tested for several hours continuously in the ambient temperature between 25 °C and 31 °C, to ensure the stability of output power. This laser has been installed at Nuclear Fuel Complex, Hyderabad for serial number marking on the end-plates of the fuel bundles. The marking depth of ~ 25 micron in Zircaloy has been achieved conforming to the NPCIL norms.



Fig.57: The photograph of the laser marker system.

V. MATERIALS SCIENCE

V.1. The generic feature of two superconducting energy gaps in superconductors with skutterudite crystal structure

The compounds with filled skutterudite structure exhibit various interesting properties including different kinds of magnetic order, superconductivity and thermal properties related to alternative technology for efficient usage and generation of energy. The temperature and magnetic field dependence of heat capacity of two such superconducting skutterudite compounds $\text{LaPt}_4\text{Ge}_{12}$ and $\text{PrPt}_4\text{Ge}_{12}$ were studied along with their electronic band structure. This study led to the finding that unlike the conventional superconductors having a single energy gap at the Fermi surface, the superconducting skutterudites possess two superconducting energy gaps at the Fermi surface.

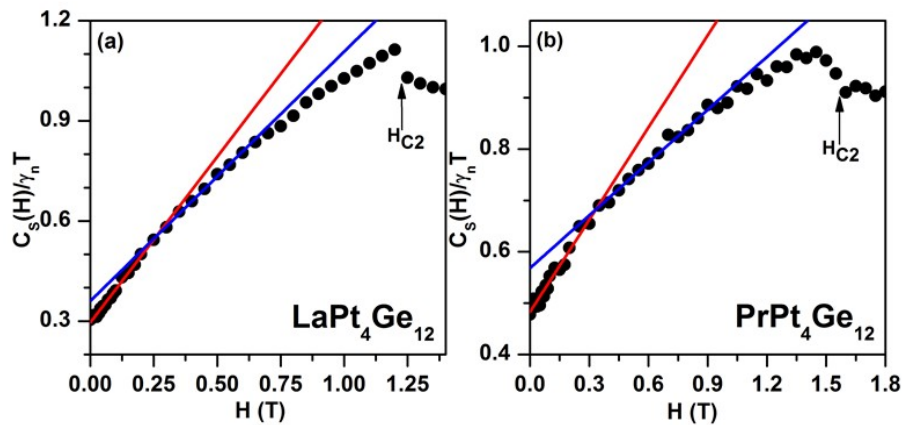


Fig. 58: Change of slope in the magnetic field dependence of (normalized) heat capacity indicating two gap superconductivity in the skutterudite compounds.

V.2. Large magnetoresistance and magnetocaloric effect in $\text{TbFe}_2\text{Al}_{10}$

The ternary magnetic compound $\text{TbFe}_2\text{Al}_{10}$ exhibits paramagnetic to ferrimagnetic and ferrimagnetic to antiferromagnetic phase transitions below 18 K. The thermal, electrical and magnetic properties of $\text{TbFe}_2\text{Al}_{10}$ were studied along with complementary magnetization measurements. The study revealed that there is a sharp rise of electrical resistivity across the paramagnetic to ferrimagnetic phase transition which is related to the occurrence of superzone boundaries at the Fermi surface. $\text{TbFe}_2\text{Al}_{10}$ also exhibits important functional properties like large magnetoresistance and magnetocaloric effect across the magnetic phase transitions which persist over a wide range of temperatures spanning deep into the paramagnetic phase.

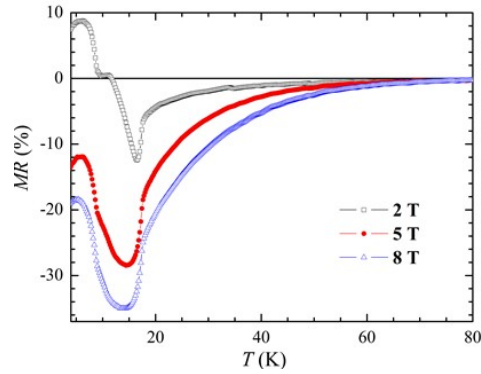


Fig. 59. Temperature dependence of magnetoresistance of $TbFe_2Al_{10}$ in different magnetic fields.

V.3. Surface oxides and their role on the optical response of high-purity niobium used in the superconducting radio frequency cavities

Fourier transform infrared and Raman spectroscopy measurements were performed on high-purity technical niobium used for the fabrication of superconducting radio frequency (SCRF) cavities. It was found that the presence of a mixture of niobium oxides and other surface impurities appreciably influence the conducting properties of the material causing it to deviate from the typical metallic characteristics. The study will provide inputs for understanding the origin of degradation of performance of the SCRF cavities during actual application.

V.4. Giant magnetocaloric effect near room temperature in Mn–Co–Ge alloy

A giant magnetocaloric effect close to room temperature was observed in an off-stoichiometric Mn-Co-Ge alloy across a first order magneto-structural phase transition. The values of isothermal entropy change are comparable or better than those found in the more expensive rare-earth based intermetallics, An experimental protocol was also devised to achieve reproducible estimates of the entropy change across a sharp first order phase transition. These results could provide useful inputs for establishing an environment friendly technology for magnetic refrigeration.

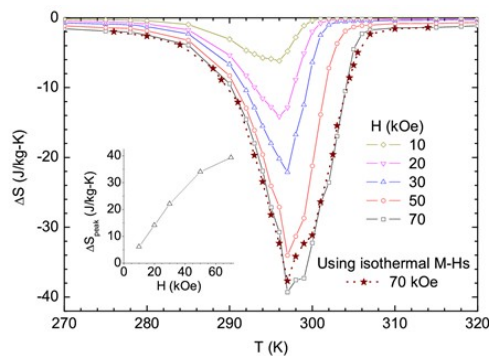


Fig.60: The magnetic entropy change as a function of temperature for various field excursions across the first order magneto-structural transition in the off-stoichiometric Mn-Co-Ge alloy.

V.5. Interesting magnetic properties observed in rare earth intermetallic ferromagnet NdRu₂

Physical properties like dc magnetization, magneto-transport and magnetostriction of C15 Laves phase 4f ferromagnetic compound NdRu₂ were investigated as a function of temperature and applied magnetic field and analyzed in a self-consistent manner. Contrary to expectation, it was found that the magnetic properties of this compound cannot be explained within a simple model based on localized magnetic moment even though Nd based compounds and alloys are usually considered as localized magnetic moment systems. These experimental results in NdRu₂ might be related with the hybridization of 4f levels with valence electrons. It is impacted that this work will stimulate experiments as well as theoretical calculations which can provide further insights on the magnetism in rare earth based intermetallic compounds.

V.6. Establishing an analogy between resistive transition in type-II superconductor with viscous flow of disordered solids

The resistive transition of vortex matter in a highly strained Nb₇₅Zr₂₅ superconducting alloy was studied. It showed that the models of viscous flow of disordered solids can be indeed applied to vortex matter. The arguments were based on purely elastic energy considerations instead of assuming any particular model applicable to the flow of flux line lattice in the mixed state of a type-II superconductor. The results show that the viscous flow of disordered solids and the flux creep phenomenon in hard type II superconductors could be the manifestation of the same underlying physical principles. These results can be of technological importance for tuning the nature of quenched disorder to achieve desirable critical current densities, and can also lead to fundamental understanding of elastic systems influenced by disorder and driven by external force.

V.7. Single Crystals and Transparent Ceramics for Laser Host and other Applications

Several high quality single crystals were grown by different techniques for various applications. These include single crystals of Nd doped GdVO₄ for laser host applications and Ce doped lithium tetra-borate (LTB) for thermos-luminescence (TL) dosimetry. A number of rare-earth doped transparent ceramics, required for laser-host and scintillation applications, have been fabricated by nano-powder technique and subsequent vacuum sintering. Transparency of ~76 % (without reflection loss correction) has been achieved at 1 μm wavelength for Nd doped YAG/Y₂O₃ and Yb,Tb co-doped Y₂O₃. For Yb, Tb co-doped Y₂O₃ ceramics a high intensity luminescence peak at 543 nm (green) was observed under 976 and 929 nm excitation due to Yb -Tb energy transfer up-conversion. Ce doped YAG transparent

ceramic was also fabricated and generation of white light was demonstrated using a blue-LED covered with this ceramic. The white light shows tristimulus values of (0.24, 0.40, 0.36). A crossover from bluish-white to greenish-yellow light was observed with an increase in the thickness of ceramic layer from 0.5 to 1.5 mm.

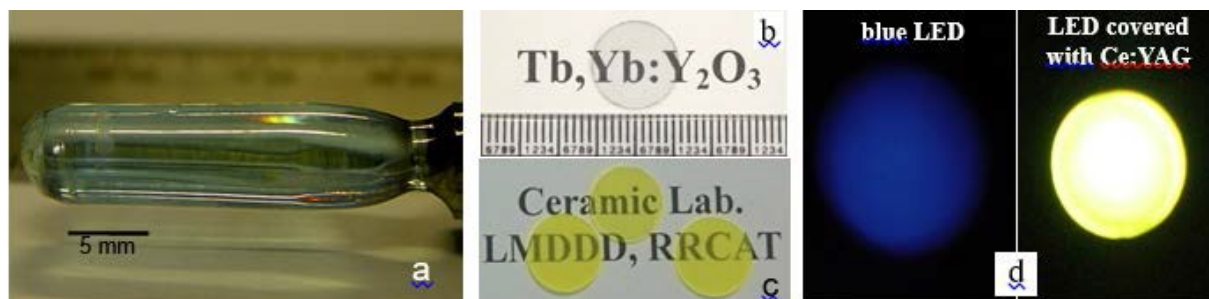


Fig. 61: (a) Single crystal of $Nd:GdVO_4$ (b) $Tb-Yb$ co-doped Y_2O_3 transparent ceramic (c) $Ce:YAG$ transparent ceramics (d) White light generation using $Ce:YAG$.

V.8. Testing of Pt-CA catalyst for D/H isotope exchange under bi-thermal condition

Dixon ring catalyst with platinum doped carbon aerogel (Pt-CA) developed under MOU between RRCAT and Heavy Water Board for hydrogen isotope exchange was tested for bi-thermal operation in an in-house developed test setup. This is an important qualifying step for bi-thermal hydrogen water (BHW) process used for heavy water production. The test setup consists of catalyst filled one meter long hot and cold columns of 1" diameter maintained under a pressure of 15 bar and at a temperature of 130 °C and 45 °C respectively. Overall extraction of deuterium in hydrogen stream from water, termed as recovery, was evaluated to be ~ 26% at 1.0 lpm of gas flow. The value compares favorably with sulphide plant with reported recovery of ~20%.

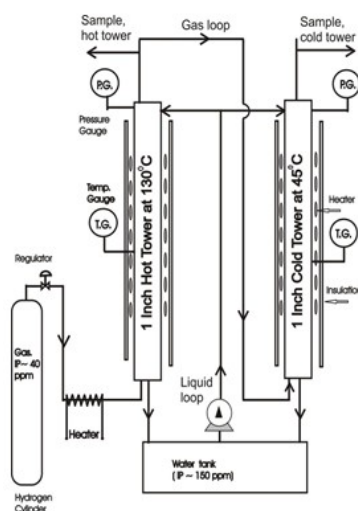


Fig 62 : Sketch of bi-thermal test

V.9. Magneto-photo luminescence : A tool for investigation of quantum structures

The photo-luminescence measurements performed on semiconductor nanostructure under high magnetic fields provide a contactless method to determine exciton properties such as effective mass, binding energy, and Bohr radius. Magneto photoluminescence (PL) experiments on AlGaAs/GaAs, InGaAs/GaAs quantum wells (QW), InAsP/InP and Type-II InP/GaAs were carried out by applying high magnetic field (8 T) at 4.2 K. The effect of carrier confinement on the effective mass of excitons and estimation of ultra-low disorder, both the interfacial and in-plane disorder, for $\text{Al}_x\text{Ga}_{1-x}\text{As}/\text{GaAs}$ multi quantum well was estimated by analyzing the line width of magneto-PL data. At the hetero-junctions, interfacial roughness is estimated to be 0.2-1.2 monolayer for $\text{Al}_{0.3}\text{Ga}_{0.7}\text{As}/\text{GaAs}$ multi QWs. This nondestructive technique for estimating ultralow disorders and effective mass is especially important since it is not possible to measure such parameters for un-doped multi QW samples by the conventional transport measurement techniques.

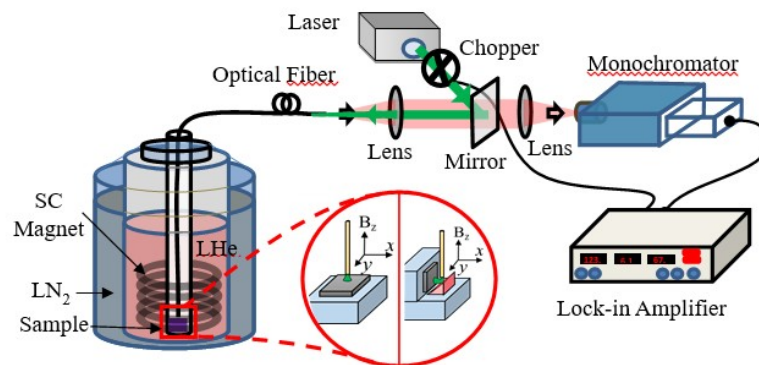


Fig. 63: Schematic of magneto-PL setup at low temperature.

V.10. Invisibility in Nanoscale: Effect on Optical Limiting:

The role of optical invisibility in curtailing the optical limiting efficiency of a nickel/toluene nanocolloid has been experimentally demonstrated for nanosecond laser pulses. The incident laser pulse heats the nanoparticle. Above a certain threshold energy the nanoparticle temperature is high enough to vaporize the solvent around it, creating a bubble. Under the right conditions this bubble can screen the nanoparticle from the incoming laser pulse. A simple yet physically realistic “particle-in-bubble” model has been developed which can quantify the linear and nonlinear absorption as well as the scattering from the sample. Such invisibility could lead to development of invisible photodetectors, densely packed devices, low-scattering near-field optical microscopes, etc.

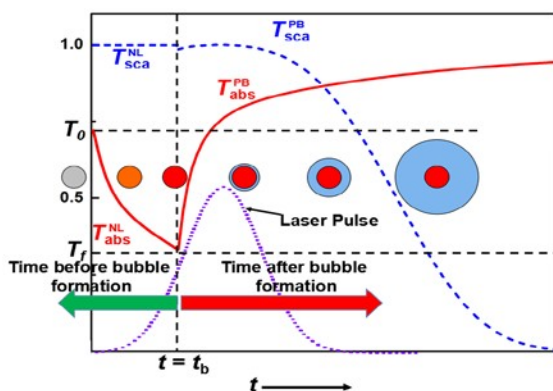


Fig. 64 : A pictorial representation of the “particle-in-bubble” model. The red circles denote the laser-heated nanoparticles and the surrounding blue spheres denote the growing bubble around the nanoparticle.

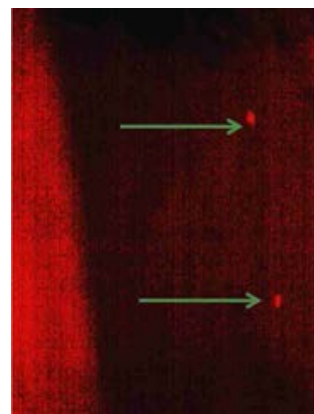


Fig. 65 : A side view image of the sample cell. The arrows show two laser-induced bubbles.

V.11. Role of plasmon resonance on quantum dot photoluminescence

Upconversion photoluminescence from quantum dots is one route to achieve microscopy resolution beyond the diffraction limit. It has been experimentally demonstrated that the upconversion photoluminescence gets strongly quenched in a CdTe quantum dot- silver nanosphere mixed nanocolloid as compared to a pure CdTe quantum dot colloid. In contrast the normal photoluminescence from the same mixture gets enhanced. This is despite a high degree of dilution in the nanocolloid sample. This behavior can be attributed to the modifications in the optical field induced by the plasmon resonance of the silver nanospheres.

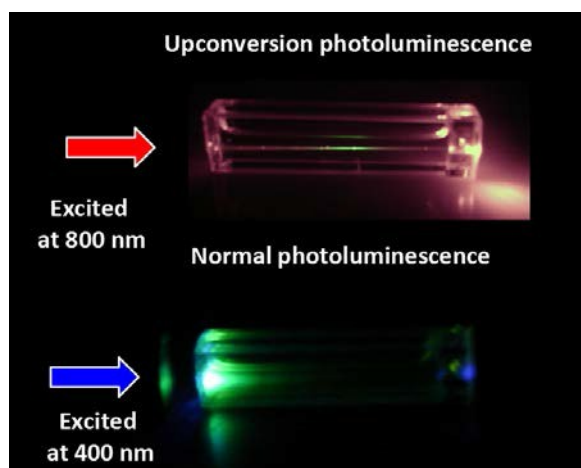


Fig. 66: Photograph showing upconversion (top) and normal (bottom) photoluminescence from CdTe nanocolloid.

V.12. Theory and computational activities

Ab initio calculations were performed to estimate electronic, mechanical, magnetic, and chemical properties of materials of potential technological interest. First-principles study of catalytic activity of subnanometer-sized bimetallic Au₁₉Pt cluster for oxidation of environmentally hazardous CO gas revealed that both CO and O₂ molecules adsorb strongly

on this cluster and O_2 gets significantly activated as compared to that on a bare gold cluster. For efficient catalysis optimum values of adsorption energy of CO and O_2 are required and these values are also estimated.

Electronic band structure studies have been used to predict that puckered SiO and CSe are direct band semiconductors with band gaps which happen to be similar to that of silicon. Planar honeycomb monolayer made up of aluminium, as that of graphene, has been shown to be stable. It is also shown that it behaves like a highly doped graphene.

Explicit effect of electron-electron correlation in Fe- and Cu-doped ZnO as well as FeGa₃ have been established from combined theoretical and Indus-based experimental studies. Novel Heusler alloys namely, Co₂PtGa and Co₂MoGa, which exhibit martensite transition as well as high spin polarization at Fermi level, have been predicted to be stable for the first time.

A computational model has been developed to elucidate the role of growth environment, impurities/additives, solvents, and their concentration to the crystallization process. It is shown that minute presence of either biuret or biurea can drastically alter the growth morphology urea crystals. In addition to this, pair creation in intense laser field has also been studied.

V.13. Light-induced synthesis of silver nanoparticles with tunable plasmonic response

Spherical and triangular silver nanoparticles with wideband plasmonic response were synthesized through a process involving liquid phase pulsed laser ablation (LPPLA) of silver target in aqueous sodium citrate solution followed by visible light irradiation. The resultant triangular nanoparticles were free from any other extraneous chemical species and exhibited high absorbance in wide wavelength band of about 550-1050 nm. This expected to be useful for trace analysis using surface enhanced Raman scattering, photovoltaics and plasmon assisted photo-catalytic studies.

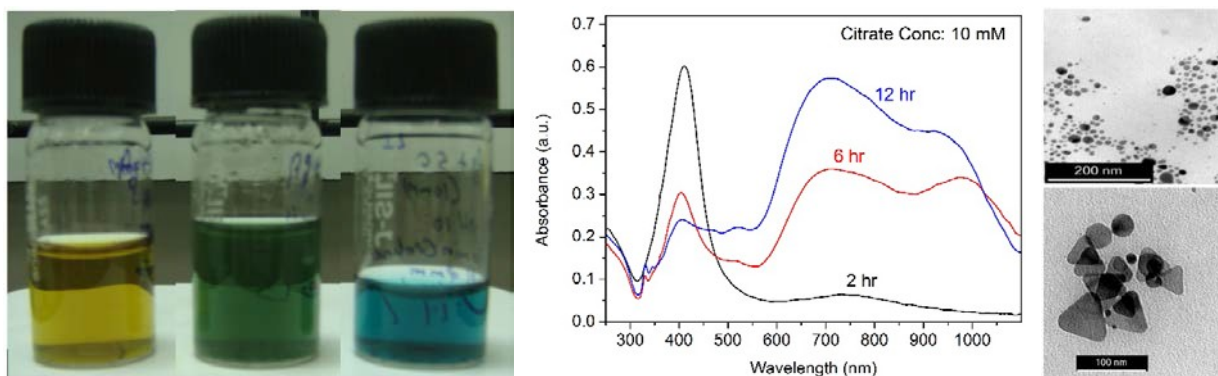
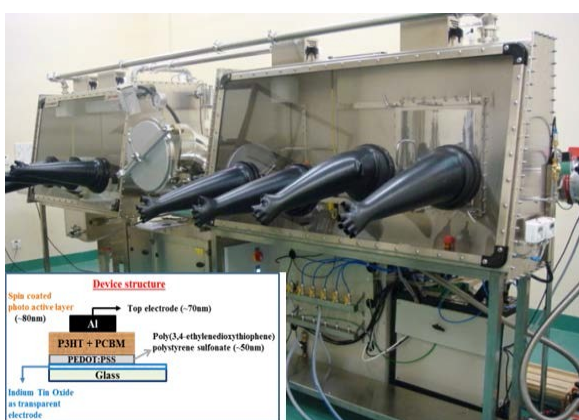


Fig. 67: Silver nanoparticle solution after 2, 6 and 12 hrs, optical absorption spectra of light irradiated silver nanoparticles (middle); TEM images LPPLA-grown silver nanoparticles before (top right) and after light irradiation (bottom right).

V.14. Fabrication of polymer based photo-voltaic cells

Using the recently procured glove box system, fabrication and characterization of polymer based photo-voltaic cells was accomplished. Composites thin films of Poly-3-hexylthiophene (P3HT) and Phenyl-C61-butyric acid methyl ester (PCBM) were used as photoactive material. The influence of thermal annealing on the device efficiency was established. The open circuit voltage (V_{oc}) of both annealed and un-annealed devices remain almost same but remarkable variation was observed in the short circuit current (I_{sc}) fill factor and η upon annealing. The observed variation upon annealing effect is due to changes in the film morphology of photoactive layer.



Device Parameters	Un-annealed	Thermally annealed (at 120 C)
V_{oc} (V)	0.63	0.62
I_{sc} (μA)	194	288
Fill factor	0.18	0.24
Efficiency, η (%)	0.53	0.98

Effect of annealing on device performance

Fig. 68: Inert atmosphere glove box system housing spin coater and thermal evaporator used for photovoltaic device fabrication. Device structure is shown in the inset.

V.15. Understanding the effect of anti phase domains (APD) in GaP/Si : A Raman and AFM microscopy study

To investigate the role of antiphase domains (APD) in generation of strain in GaP film grown on different substrates, GaP/Si and GaAs heterostructure are studied using Raman spectroscopy along with atomic force microscopy. It is concluded that the APD are predominant at the valley region of the surface morphology in GaP/Si, which is the main reason for lower growth rate at the valley region. The information obtained using spatially resolved Raman spectroscopy is very useful for identification of high density APD regions in the III-V semiconductor layers grown on Si/Ge.

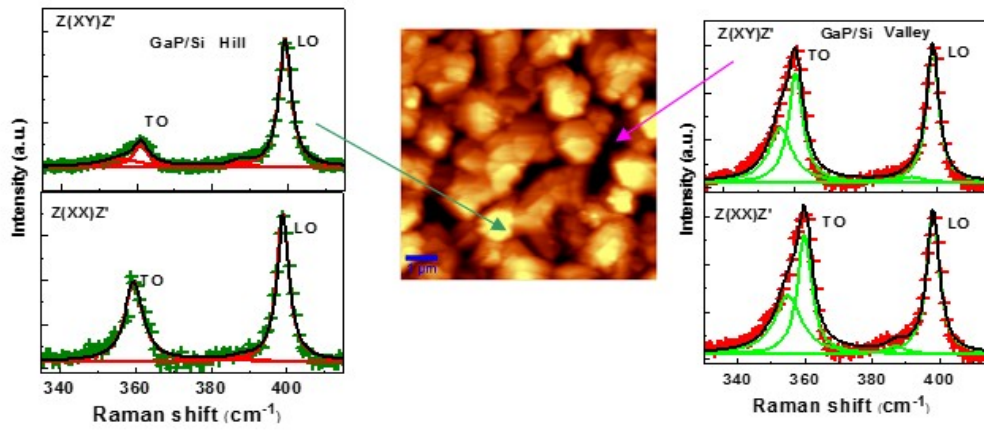


Fig. 69: Raman spectra and AFM image of the GaP/Si sample showing the following of Raman selection rules in island region and deviation from the Raman selection rule in valley region. $Z(XX,XY)Z'$ represent Raman data in back scattering (Z' direction) configuration with incident light polarization chosen to be in X and scattered light polarization are chosen in ' X ' and ' Y ' directions respectively.

VI. INTERNATIONAL COLLABORATION

VI.1. Contribution to International Collaborations

As a part of the in-kind contribution to Facility for Antiproton and Ion Research (FAIR), Darmstadt, Germany over 500 power converters for electromagnets will be designed, developed and supplied. The first converter of this series, a two-quadrant converter (300 A / ± 142 V), has been developed based on the design and prototyping provided by RRCAT, Indore at ECIL, Hyderabad. The converter has qualified factory acceptance tests and has been delivered to FAIR for site acceptance tests. Subsequently, production of 50 such power converters will commence at ECIL. Figure 70 shows the power converter.



Fig. 70: A photograph showing the power converter for electromagnet developed for FAIR.

VI.2. Development of power couplers under DAE-CERN collaboration

RRCAT has successfully developed, tested and supplied two high power WR 2300 copper coated stainless steel power couplers for CERN's linac-4 project. RRCAT scientists participated in the commissioning of the accelerating structures and the beam diagnostics for the linac 4. The linac-4 has been commissioned by CERN and accelerated H⁻ ions to the rated energy of 160 MeV.

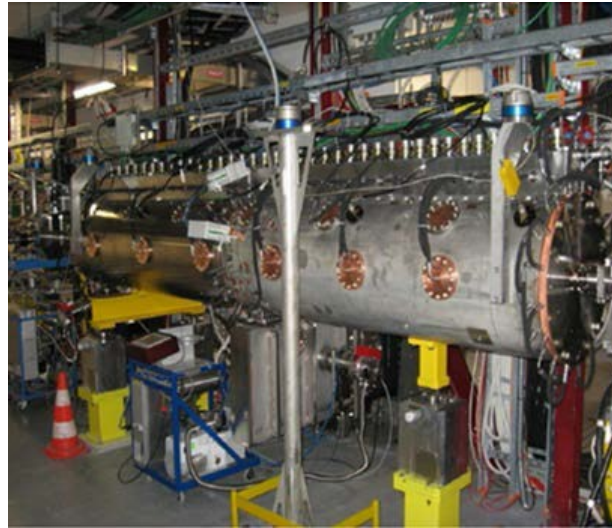


Fig 71. One of the WR 2300 copper coated Stainless steel power couplers installed with the CCDTL accelerating structure of linac-4 tunnel at CERN.

VII. INFRASTRUCTURE

VII.1. Computing infrastructure

Various software applications were developed and deployed in an endeavour to push e-Governance at RRCAT. These include digital signature based casual entry permit, material gate pass management etc. RRCAT web site was upgraded to latest platforms and webpages for CHSS beneficiaries, suppliers and pensioners were also added. A vehicle movement monitoring system based on UHF technology has been deployed at Guard House security. Integration of Kshitij-4 high performance computing cluster with centralised resources was accomplished and it was released to users for regular use.

VII.2. Civil infrastructure

Design and construction of accelerator component design and fabrication shop (ACDFS) lab building, pre-engineered building for ACDFS, cryo-module development lab, 132 kVA substation, lift block for RRCAT guest house, barracks & armory for CISF, lakeside community center, and extension of RRCAT medical physiotherapy center have been completed.



Fig. 72: Pre-engineered building for ACDFS



Fig. 73: View of lakeside community center.



Fig. 74: CISF barracks.



Fig. 75: CISF armory.

VIII. HUMAN RESOURCE DEVELOPMENT

VIII.1. Human resources development based activities

Human resources development activities at RRCAT were continued and contributed in a significant way towards development of quality manpower in the form of imparting training to Trainee Scientific Officers (TSOs) in the discipline of physics, electrical and electronics, providing one year pre-doctoral course work towards the successful completion of Ph.D. degree of HBNI, Mumbai. In addition RRCAT provide guidance to M.Tech/M.Sc. students to carry out their one year/six months project work towards the partial fulfilment of their degrees. In the 16th batch, 5 TSOs have completed the one year orientation course in the field of Accelerators and Lasers and have been placed in various units of DAE. In the current 17th batch, 5 TSOs are undergoing training. 5 TSOs who passed out previously from various BARC training schools and joined RRCAT as SO/C have been awarded M.Tech. degree. Number of Ph.D. scholars who have completed the one year pre-doctoral course are 9 and currently 7 Ph.D. scholars are undergoing the course work. During 2015-16, 8 scholars have been awarded Ph.D. degree by HBNI. A total number of 110 students from various universities/institutions have completed their M. Tech project work at RRCAT

IX. OUTREACH ACTIVITIES

IX.1. The six week Orientation Course on Accelerators, Lasers and related Science and Technologies (OCAL-2016) was successfully conducted during 23 May - 15 July, 2016.

In all, 39 post-graduate students (M.Sc., M.Tech./M.E.) from 16 states attended the course which comprised lectures, invited talks, hands-on experiments, visits to RRCAT laboratories, students' seminar and an industrial unit. All students completed the course successfully and were awarded certificates by Shri K.N.Vyas, Director, BARC and Member, AEC. RRCAT participated in three national events by setting up an exhibit at the 103rd Indian Science Congress held at Mysore during Jan 3-7, 2016, the 2nd India International Science Festival (IISF) - 2016 organized at the CSIR-NPL, New Delhi during Dec 7-11, 2016 and the National Vender Development Programme doing MSME convention at Bhopal during Oct 1- 2, 2016.

IX.2. National Science Day was celebrated on 27 February, 2016. More than 1500 students and teachers of 110 schools from Indore and nearby places, and nearly 2000 members of public visited scientific facilities in RRCAT. This year a gallery 'Make in India' science and technology was also established to showcase the indigenous scientific and technological achievements RRCAT. This was well appreciated.

During the past year several visits of school and college students, teachers, and professionals from other organizations were organized where the visitors were taken around the RRCAT laboratories. This include the Vigyan Manthan Yatra for 125 students from various schools of M.P. selected by Madhya Pradesh Council of Scientific and Technology.



Fig. 76: Dr. D. K. Shrivastava addressing the audience during the inauguration function of OCAL 2016.



Fig. 77: Participating students of OCAL 2016 with the dignitaries and members of the Public Outreach Committee.

X. RTI DETAILS

The number of RTI applications received and disposed of during January to December 2016 are given below.

Month	No. of RTI applications received	No. of applications disposed of
January	15	13
February	15	15
March	12	09
April	06	06
May	06	06
June	05	02
July	09	09
August	10	06
September	07	08
October	10	07
November	05	09
December	07	06
Total	107	97